ARTICLE

https://doi.org/10.1038/s41586-019-1294-0

Antarctic offshore polynyas linked to Southern Hemisphere climate anomalies

Ethan C. Campbell[1]*, Earle A. Wilson[1], G. W. Kent Moore[2,3], Stephen C. Riser[1], Casey E. Brayton[4], Matthew R. Mazloff[5] & Lynne D. Talley[5]

Offshore Antarctic polynyas—large openings in the winter sea ice cover—are thought to be maintained by a rapid ventilation of deep-ocean heat through convective mixing. These rare phenomena may alter abyssal properties and circulation, yet their formation mechanisms are not well understood. Here we demonstrate that concurrent upper-ocean preconditioning and meteorological perturbations are responsible for the appearance of polynyas in the Weddell Sea region of the Southern Ocean. Autonomous profiling float observations—collected in 2016 and 2017 during the largest polynyas to form near the Maud Rise seamount since 1976—reveal that the polynyas were initiated and modulated by the passage of severe storms, and that intense heat loss drove deep overturning within them. Wind-driven upwelling of record strength weakened haline stratification in the upper ocean, thus favouring destabilization in 2016 and 2017. We show that previous Weddell polynyas probably developed under similarly anomalous conditions, which are associated with a mode of Southern Hemisphere climate variability that is predicted to strengthen as a result of anthropogenic climate change.

The blanket of sea ice that develops around Antarctica each winter reduces interaction between the ocean and the atmosphere. By eliminating this barrier, large offshore openings in the sea ice pack—sometimes referred to as 'open-ocean' or 'sensible heat' polynyas—expose the ocean surface to heat extraction by the frigid atmosphere above. The resultant loss of surface buoyancy may drive convective overturning, maintaining ice-free conditions by liberating vast amounts of heat stored precariously just below the cold surface layer[1–3]. These deep mixing events may rapidly modify the ocean interior, with far-reaching implications for abyssal properties[4], large-scale ocean circulation[5–10] and carbon sequestration[11,12]. Further, heat ventilation during offshore polynya events can be expected to affect the regional atmospheric state[9,13,14] and possibly global climate patterns through atmospheric teleconnections[15].

The Antarctic Bottom Water that fills the global abyss today originates from the Antarctic continental margin[16]. However, in past glacial climates[16,17]—when grounded ice sheets restricted formation at present-day sites—and perhaps even in pre-industrial times[18,19], it may have been formed predominantly in offshore polynyas. This offshore deep water formation pathway is spuriously prevalent in many present-generation climate models, and introduces biases into the present and future Southern Ocean properties, circulation, and sea ice area[8,20–22]. In contrast to climate models, the modern satellite record (1972–present) shows only intermittent occurrence of offshore polynyas, the largest of which have appeared in the Weddell Sea region near the Maud Rise seamount and in the Cosmonaut Sea offshore of East Antarctica[23]. In the most prominent example, early satellite observations revealed massive, persistent Weddell polynyas over three consecutive winters from 1974 to 1976[24] (Fig. 1a). Despite an absence of in situ ocean measurements during these events, bottom-reaching mixing within the polynyas was inferred from a hydrographic survey in 1977, which discovered erosion of normal temperature and salinity layering in one location[1].

Shorter-lived, smaller openings have recurred near Maud Rise[23,25], with the largest reappearances in 2016 and 2017[10,26] (Fig. 1). Notably, the 2016–2017 polynyas accompanied a reversal of the positive trend in Antarctic sea ice extent that has been observed over the past three decades[27,28], which raises the possibility that the Maud Rise events may reflect a larger climate signal[10]. The tendency of polynyas to emerge near the seamount is not a coincidence. Theory, model simulations and sparse observations suggest that topography–flow interactions at Maud Rise enhance upward heat fluxes and generate eddies that transmit divergent strain to the ice cover[25,29–32] (see ref. [32] for a comprehensive discussion of related mechanisms). However, the intermittency of openings remains unexplained. More generally, the absence of detailed measurements of an offshore polynya has afforded little opportunity to validate the local processes and climate influences that have been put forward to explain how destabilization, polynya formation and possibly deep overturning may occur within the ice-covered gyres of the Southern Ocean.

Here we present the first comprehensive analysis of the ocean, ice and atmosphere during an offshore Antarctic polynya event. Passive microwave sea ice concentration (SIC) data and ERA-Interim (ERA-I) reanalysis fields depict the evolution of ice and atmosphere in 2016 and 2017 (Figs. 2a, 3a, b), whereas three under-ice profiling floats—purposefully trapped in the rotating Taylor column circulation over Maud Rise[31] (Fig. 1b, c)—together provide a continuous record from 2011–2018 (Fig. 4). Two of these floats, deployed as part of the Southern Ocean Carbon and Climate Observations and Modeling (SOCCOM) Project, were present during the 2016–2017 polynya events. A synthesis of almost 4,000 past hydrographic observations from floats, ships and instrumented seals near Maud Rise provides year-round climatological baselines, against which 2016 and 2017 may be compared (Extended Data Fig. 1; Methods section 'Hydrographic climatologies'). Lastly, a new record of past offshore polynyas reveals connections to large-scale climate fluctuations (Fig. 5).

Polynya formation in 2016

On 27 July 2016, a month after ice formed over Maud Rise, a sliver of open water appeared above its northeast flank (Fig. 2a, Extended Data Fig. 2), which is a location that is predisposed for reduced SIC[25,30,32].

[1]School of Oceanography, University of Washington, Seattle, WA, USA. [2]Department of Physics, University of Toronto, Toronto, Ontario, Canada. [3]Department of Chemical and Physical Sciences, University of Toronto Mississauga, Mississauga, Ontario, Canada. [4]School of the Earth, Ocean and Environment, University of South Carolina, Columbia, SC, USA. [5]Scripps Institution of Oceanography, University of California San Diego, La Jolla, CA, USA. *e-mail: ethancc@uw.edu

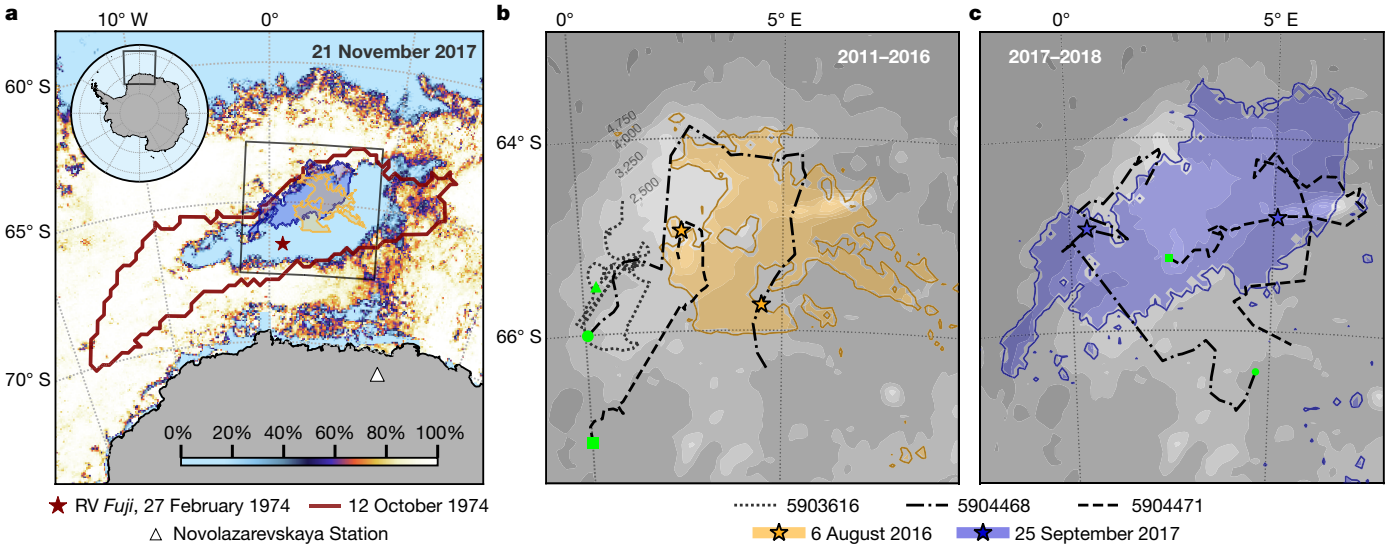

Fig. 1 | Polynyas of 1974, 2016 and 2017 in relation to profiling float trajectories near Maud Rise. a, Sea ice concentration in the eastern Weddell sector of the Southern Ocean on 21 November 2017 from AMSR2-ASI, overlaid with 50% SIC contours showing polynya extent on 12 October 1974 (from Nimbus-5 ESMR; red contour) as well as on 6 August 2016 and 25 September 2017 (from AMSR2-ASI; orange and blue shading). The grey box encompasses the area shown in **b** and **c**. The red star identifies the MLS measurement obtained by research vessel (RV) *Fuji* on 27 February 1974 (shown in Fig. 2b)[41], and the white triangle marks Novolazarevskaya Station, Queen Maud Land (see pressure record in Fig. 5c). **b**, Bathymetry around Maud Rise (depth contours labelled in metres) with polynya extent from 2016 shaded as in **a**. Trajectories of floats 5903616 (December 2011 to June 2016), 5904468 (January 2015 to December 2016) and 5904471 (December 2014 to December 2016) begin at deployment locations (green) and include estimated locations during the 2016 polynya (orange stars). **c**, Bathymetry as in **b** with polynya extent from 2017 shaded as in **a**. Trajectories of floats 5904468 (January 2017 to May 2018) and 5904471 (January 2017 to June 2018) begin at marked locations (green) and include estimated locations during the 2017 polynya (blue stars). See Extended Data Figs. 2, 8 for full evolution of SIC during the 2016 and 2017 polynyas with float locations.

Despite below-freezing air temperatures, the polynya eventually expanded to 33,000 km^2 (Fig. 3a, Extended Data Fig. 3b), making it the largest opening from full ice cover since 1976 (Fig. 5a). The polynya closed 21 days later, on 17 August 2016 (Fig. 3a, Extended Data Fig. 2). An exceptionally rapid melt season across all Antarctic sectors followed in November. Although most explanations for this unprecedented sea ice retreat have focused on the variability in atmospheric circulation associated with tropically forced teleconnections (refs [27,28] and references therein), wind-driven upwelling of warm subsurface water may have also contributed in some regions[28].

Profiling float data near Maud Rise show that a late freeze in 2016 (Fig. 2a) followed 4–5 months of increased mixed-layer temperature (Extended Data Fig. 3d) and mixed-layer salinity (MLS; Fig. 2b). These anomalies are consistent with strengthened upwelling and entrainment of Weddell Deep Water, which is warmer and saltier than the overlying upper ocean (Fig. 4a, b). Abnormal ocean conditions persisted into the period of ice formation. Early July featured the two highest MLS measurements in our eastern Weddell record for that month, which correspond to a maximum elevation of MLS above the Maud Rise climatology of +0.12 practical salinity units (psu) (Fig. 2b).

We attribute the 2016 polynya primarily to preconditioning from these salinity anomalies. Under sea ice, stratification is governed by fluctuations in MLS. The special vulnerability of the Maud Rise water column to overturning is in part due to its high climatological MLS relative to that of the surrounding region[29] (Fig. 2b). In a normal winter, brine rejection from ice growth over Maud Rise brings the pycnocline to the brink of erosion[33]. Complete destabilization, however, is averted through entrainment of warm thermocline water as the mixed layer deepens. Ventilation of this 'thermal barrier' into the mixed layer suppresses ice growth, providing a negative feedback that preserves stratification[3,33–36]. However, by mid-July 2016, an increase in MLS of just 0.05 psu would have eliminated stratification and triggered deep convection (red line in Fig. 2b), less than a third of that required in a normal year.

In this precarious state, we infer that intense storms overrode the stabilizing negative feedback and initiated deep convection by providing two sudden perturbations: ice divergence and enhanced turbulent mixing. Divergence may occur across a continuum of spatial scales owing to ice deformation and drift[37], and enables rapid ice growth and brine rejection while preventing immediate stabilization from ice melt. Wind-driven turbulent mixing entrains heat and salt into the mixed layer[34], a response that is amplified under weak stratification[33]. The heat may melt ice, as idealized model experiments with storm perturbations have demonstrated for the Maud Rise ice–ocean system[33]. Although ice may reform, negating the stabilizing buoyancy input of melt, entrained salt will linger and will reduce stability[3,34,35]. These perturbations have been observed to co-occur: during a 1994 winter field campaign over Maud Rise, two violent storms elevated mixed-layer temperature by 0.3 °C above freezing and opened leads that forced an evacuation of the researchers' ice camp[38]. Young, possibly thinner ice in July 2016 would have been particularly susceptible to wind forcing[37], which would enhance both mechanisms.

Using atmospheric reanalysis, we identify the passage of the most severe cyclones near Maud Rise (see Methods section 'Storm identification'). Most storms coincide with marked reductions in average SIC (Fig. 2a, Extended Data Fig. 4). Indeed, the 2016 polynya opened during a storm that featured 10-m wind speeds of up to 25 m s^{-1} and surface pressures as low as 947 hPa (Fig. 3a, Extended Data Fig. 4a). We find a surprising correspondence ($r = 0.81$) between the evolution of the extent of the polynya in 2016 and the cumulative wind-speed anomaly from a baseline value (Fig. 3a), which indicates that the polynya grew with strong winds from storms and shrank during quiescent periods. Along its ice-covered perimeter, high winds may have triggered ice loss and destabilization through turbulent mixing. Within its interior, heat extraction and salty turbulent entrainment from high winds would have driven convection, preventing ice from reforming. During a storm on 2 August, the polynya expanded concurrently with ocean–atmosphere turbulent heat fluxes of up to 718 W m^{-2} (Fig. 3b, c) and possible ice divergence (Extended Data Fig. 5). A lapse in storm activity and a reduction in heat flux apparently enabled the polynya to close (Fig. 3a, c). Nonetheless, MLS remained near the overturning limit throughout the winter (Fig. 2b). A storm on 28–30 August caused substantial SIC reduction and warm entrainment (Extended Data Figs. 3d, 4a), and in

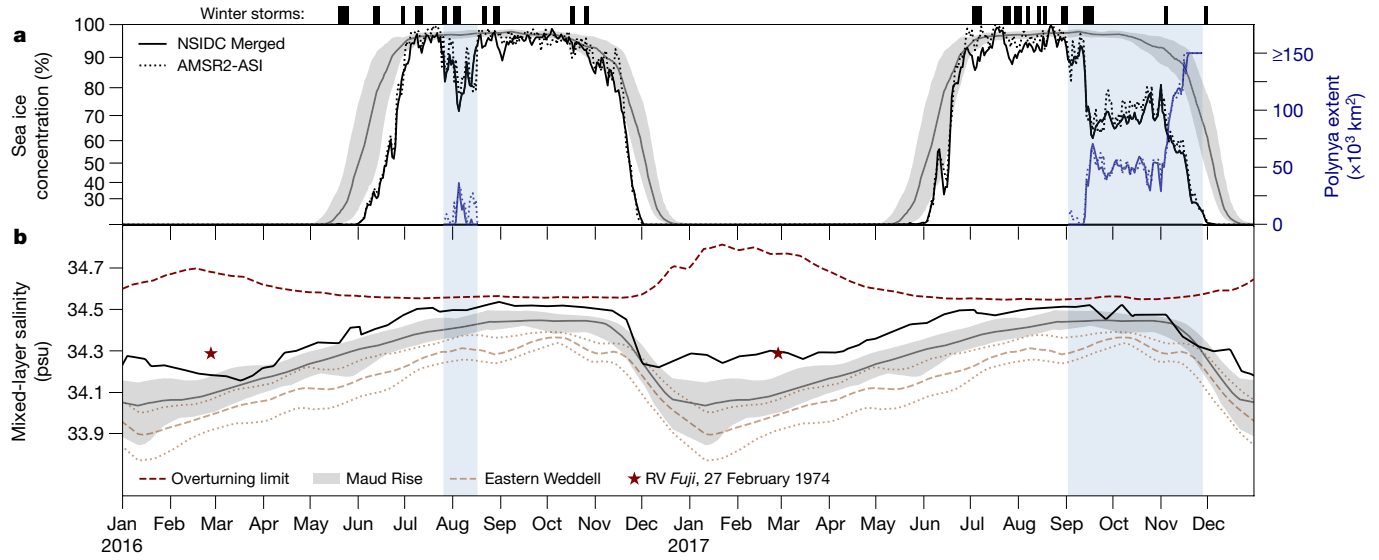

Fig. 2 | Storms, sea ice concentration and mixed-layer salinity at Maud Rise in 2016 and 2017. Marked at the top are intense winter storm events near Maud Rise (also see Extended Data Fig. 4 and Methods section 'Storm identification'). **a**, Average daily SIC within the Maud Rise region (63°–67° S, 0°–10° E) from NSIDC Merged (solid black line) and AMSR2-ASI (dashed black line) in 2016 and 2017. SIC climatology from NSIDC Merged (1978–2019) is shown as median (grey line) and 25%–75% interquartile range (IQR; grey shading). Note the stretched *y* axis. Polynya extent is quantified (blue lines) during the 2016 and 2017 events (vertical blue shading). **b**, Composite of the highest MLS measured by floats 5903616, 5904468 and 5904471 in 2016 and 2017 (black line; see Methods sections 'Derived oceanographic quantities' and 'Composites of float time series'). MLS climatology for the Maud Rise region ($R < 250$ km from 65° S, 3° E) is shown as median (grey line) and IQR (grey shading); climatology for the eastern Weddell region away from Maud Rise ($250 < R < 500$ km) is presented for comparison (light brown dashed and dotted lines for median and IQR, respectively; see Methods section 'Hydrographic climatologies'). Red stars indicate the MLS measured by RV *Fuji* on 27 February 1974 at 66.5° S, 1.2° E, near Maud Rise[41] (see red star in Fig. 1a). The MLS required to eliminate 0–250 m stratification, the 'overturning limit', is shown in red (see Methods section 'Composites of float time series').

late October—after two storms (Fig. 2a)—a distinct polynya appeared south of Maud Rise, and eventually grew during climatological melt to encompass much of the eastern Weddell (Extended Data Fig. 2).

Deep mixing and resultant preconditioning

We observe an abrupt appearance of anomalies in the ocean interior after the opening of the 2016 polynya: cooling of 0.2 °C, freshening of 0.025 psu, and an increase in dissolved oxygen of 10 μmol kg^{-1} at a depth of around 650 m (Fig. 4a–c, Extended Data Fig. 6). Co-located with these modified patches are bands of near-zero buoyancy frequency (N), which indicate nearly absent stratification (Fig. 4d). These properties reflect recent mixing with winter surface water, as observed during open-ocean convection in the subpolar North Atlantic[39]. The apparent strengthening and deepening of interior mixed layers after the polynya—observed by both floats (Extended Data Fig. 6)—suggest lateral mixing and homogenization of remnant convective plumes, which probably evolved on scales missed by the coarse sampling in space and time (see Methods section 'Derived oceanographic quantities'). The isolated intrusion from 500 m to 800 m, which is embedded within displaced isotherms and isohalines (Fig. 4a, b), resembles the submesoscale coherent vortices that are frequently observed after open-ocean convection, such as in the Mediterranean Sea[40]. Together these fingerprints identify the altered water mass as the product of deep-reaching convective mixing.

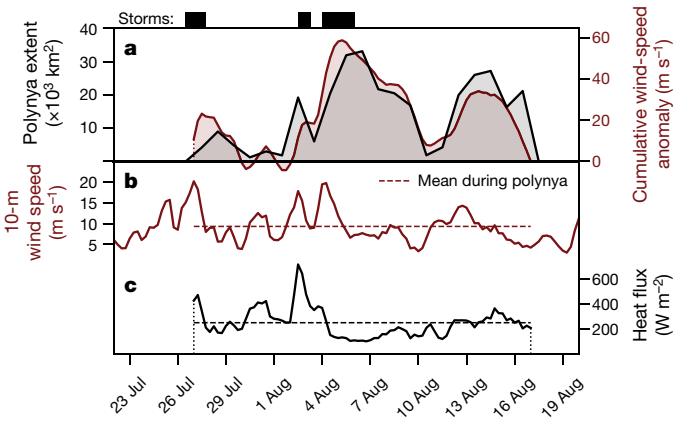

Fig. 3 | Local meteorology and heat loss during the 2016 polynya. Intense winter storm events near Maud Rise are identified at the top, as in Fig. 2. **a**, Daily polynya extent from AMSR2-ASI (see Methods section 'Polynya identification') is shaded in black. Overlaid in red is the cumulative sum of the anomaly of 10-m wind speed (as shown in **b**) from its mean value during the 2016 polynya. **b**, Average six-hourly 10-m wind speed from ERA-I reanalysis within the Maud Rise region (63°–67° S, 0°–10° E). **c**, Average six-hourly ocean-atmosphere turbulent heat flux within the polynya (see Methods section 'Atmospheric reanalysis'). Dashed lines indicate mean values during the polynya event.

Analysis of the reduced deep heat content in post-polynya profiles yields estimated ventilation rates (Methods section 'Polynya heat flux estimates') that approach the average ocean–atmosphere turbulent heat flux during the 2016 polynya (252 W m^{-2}; Fig. 3c, Extended Data Fig. 7). This close correspondence suggests that deep convection was driven primarily by a continuous loss of surface buoyancy, rather than by the interior thermobaric mixing that has been invoked to explain overturning near Maud Rise[36]. Persistent above-freezing mixed-layer temperature provides additional evidence for continuous thermal convection (Extended Data Fig. 3d). Nonetheless, thermobaricity may have modulated the depth of mixing by supplying additional kinetic energy to plumes descending across the pycnocline.

Crucially, the deep freshening that accompanied heat loss in 2016 implies a net upwards mixing of salt[41], thus reducing stability in 2017. This upwards transfer is corroborated by an increase in total salt content from 0 m to 250 m—equivalent to the effect of brine rejection from 0.46 m of ice formation (Extended Data Fig. 3e)—as well as an average MLS elevation of 0.15 psu over the ice-free months of 2017 (Fig. 2b).

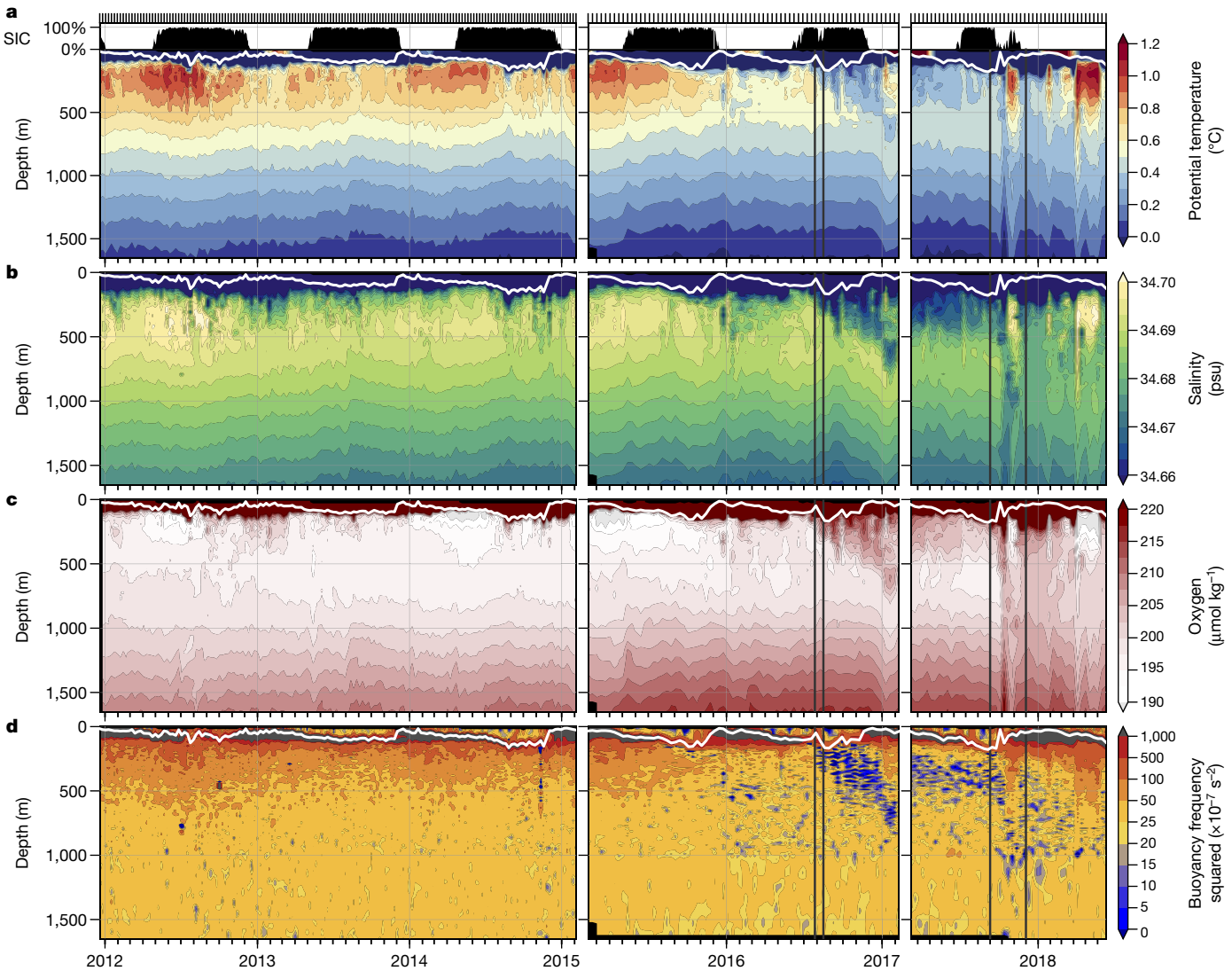

Fig. 4 | Hydrographic observations from Maud Rise from 2011–2018. **a**–**d**, Continuous-time depth sections of potential temperature (**a**), salinity (**b**), dissolved oxygen (**c**) and buoyancy frequency squared (N^2) (**d**) assembled using observations from profiling floats 5903616 (left), 5904468 (centre) and 5904471 (right). Individual profiles are marked at the top (black ticks). Mixed-layer depth is indicated in white. Vertical lines in each panel mark the start and end dates of the 2016 and 2017 polynyas. Along-trajectory SIC, primarily from AMSR2-ASI, is shaded at the top in black (see Methods section 'Sea ice concentration data'). See Extended Data Fig. 6 for the complete time range of data from each float.

This extreme degree of preconditioning is comparable to that observed near Maud Rise before the 1974 polynya[41] (red stars in Figs. 1a, 2b).

Polynya recurrence in 2017

Low upper-ocean stability in early 2017 preconditioned the region for the emergence of a larger polynya than that formed in 2016 (Fig. 1). In July and August, SIC and upper-ocean salt content were highly variable (Fig. 2a, Extended Data Fig. 3e), indicating cycles of melt and refreeze consistent with a strengthened negative feedback to ice growth and a weakly stabilizing buffer from thin ice. Indeed, we estimate that net in situ ice growth in 2017 was half of that experienced in a normal winter (Extended Data Fig. 3e). On 27 July, after four days of storm activity, numerous scattered, short-lived polynyas appeared southwest of Maud Rise. Later, on 3 September, two larger openings emerged above the seamount during a brief storm; they then merged and rapidly grew after storms from 13 to 18 September, which featured the highest wind speeds seen in reanalysis that winter (Fig. 2a, Extended Data Figs. 4b, 8). Within this expanding polynya, both floats inferred ice-free conditions from prolonged warm near-surface temperatures and surfaced to transmit data—a highly unusual occurrence (Extended Data Fig. 8; see Methods section 'Hydrographic data'). A 1.5-month lull in storm activity saw the extent of the polynya stabilize at around 50,000 km^2, before seasonal ice melt and coalescence with the open ocean occurred in November (Fig. 1a, c, 2a, Extended Data Fig. 8).

In October 2017, a near-homogeneous cold, fresh and high-oxygen coherent structure, spanning depths from around 200 m to 1,700 m, was detected from within the polynya. The development of such a structure indicates deeper and more vigorous convection than in 2016 (Fig. 4a–c). As with the remnant 'chimney' observed in 1977[1], normal ocean layering was absent. Whether mixing extended below 1,700 m in 2017 cannot be determined from the float data, but we note that the low interior stratification offers little resistance to convection (Extended Data Fig. 6e). This raises the possibility that smaller, shorter-lived polynyas may introduce modification to a similar depth as the 1974–1976 events. However, mixing within transient polynyas near Maud Rise need not be bottom-reaching to affect the properties of the abyssal world ocean. Counterintuitively, bottom water masses remain mostly topographically confined to the Weddell Basin, whereas deep and intermediate layers outflow and spread northwards as Antarctic Bottom Water (refs [42,43] and references therein). Even brief polynyas may have an outsized effect. Total heat loss during the 21-day opening in 2016 was approximately equal to that which occurs during a

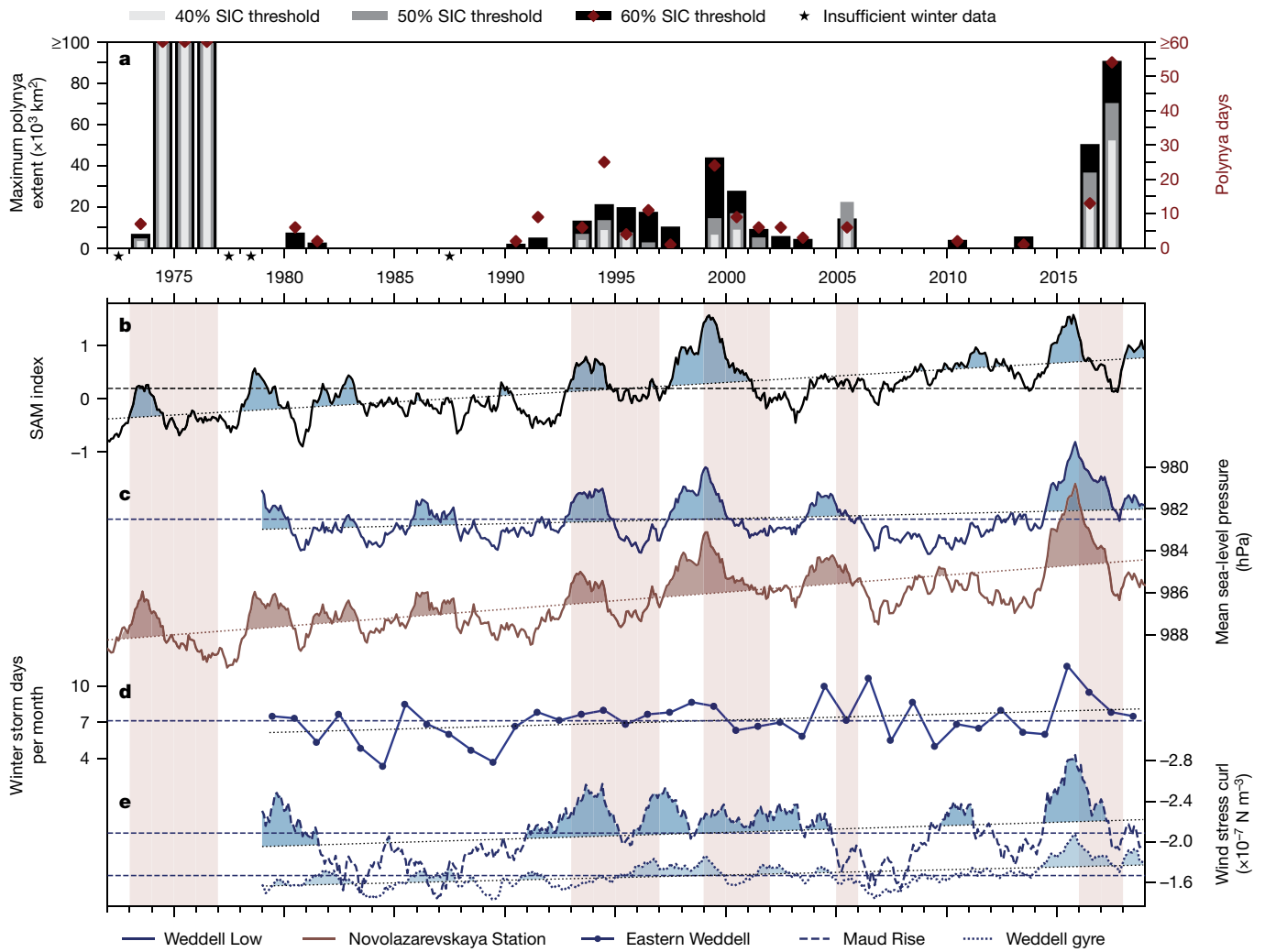

Fig. 5 | Relationships between past polynyas near Maud Rise and climate forcing from 1972–2018. a, Annual maximum polynya extent (bars) and number of polynya days (red diamonds; see Methods section 'Polynya identification'). Maximum polynya extent is calculated for three SIC thresholds representing increasingly strict polynya definitions: 60%, 50% and 40%. Polynya days are quantified using the 60% threshold. Stars indicate years with incomplete or absent SIC records. **b**, SAM index for the years 1972–2018. **c**, Mean sea-level pressure from ERA-I reanalysis, for 1979–2018, within the Weddell Low region (blue; see Methods section 'Weddell Low'), and from Novolazarevskaya Station, Queen Maud Land, for 1972–2018 (brown; see white triangle in Fig. 1a and Methods section 'Meteorological station records'). Note the reversed *y* axis. **d**, Eastern Weddell region (62°–68° S, 15° W–20° E) winter (May–October) mean storm days per month (see Methods section 'Storm identification'). **e**, Average wind stress curl from ERA-I over Maud Rise (63°–67° S, 0°–10° E; dashed) and the entire Weddell gyre (60° S to the Antarctic continent, 60° W–45° E; dotted). Time series in **b**, **c** and **e** are filtered using a two-year centred running mean and shaded above their linear trends to highlight longer-term fluctuations. See Extended Data Table 1 for trends and significance for **b**–**e**. Horizontal dashed lines are mean values. Years with polynya activity at the 50% threshold are shaded vertically in red in **b**–**e**.

normal ice-covered winter[29], thus accelerating the transformation of circumpolar-derived Weddell Deep Water on its slow transit through the Weddell gyre[43].

Role of climate variability

Although 2016 and 2017 were exceptional, transient polynyas near Maud Rise have also occurred in clusters of years from 1993–1996 and 1999–2001, as well as in 2005 (Fig. 5a). This is in line with sequences of polynya years found in a high-resolution model simulation of the region[32]. We have shown that the recurrence of polynyas may be explained by upward salt transfer from convective mixing. However, what controls the intermittency of initial openings is still unknown. By examining climate records from 1972–2018 to identify a common mechanism, we find that the Southern Annular Mode (SAM)—the leading mode of variability in the Southern Hemisphere[44]—fluctuates in lockstep (Fig. 5b, c, Extended Data Table 1) with indices of mean sea-level pressure for the Weddell Low, the climatological low surface pressure centre east of Maud Rise ($r = -0.71$; see Methods section 'Weddell Low'), and from Novolazarevskaya Station, south of Maud Rise ($r = -0.82$; see white triangle in Fig. 1a). In turn, the curls of wind stress over both the entire Weddell gyre and Maud Rise are correlated with the Weddell Low ($r = 0.61$ and 0.48, respectively; Fig. 5c, e). Also correlated with the Weddell Low is the frequency of severe winter storms within the eastern Weddell region ($r = -0.55$; Fig. 5d). These relationships are analogous to those associated with variability of the Amundsen Sea Low[45].

Figure 5 illustrates that past transient polynyas near Maud Rise were preceded by synchronous deviations in these indices: positive SAM, deeper Weddell Low, strengthened cyclonic wind stress curl and frequent winter storm activity. Notably, there were more than twice as many winter storms in 2015 and 2016 as occurred in the least stormy years (Fig. 5d). We have suggested that intense storms facilitate ice loss through turbulent mixing and ice divergence. The other large-scale anomalies provide the preconditioning necessary to permit a polynya in the first place[2]. Local wind stress curl is a proxy for ocean upwelling velocity due to the Ekman relation, and modelling and

theoretical studies indicate that enhanced upwelling favours polynya development by concentrating warm, salty Weddell Deep Water closer to the surface[2,6,32,33,35,46]. Perhaps more important, however, are the salinity fluxes into the mixed layer that are associated with upwelling. Record-strong wind stress curl in 2015 and 2016 (Fig. 5e) increased MLS near Maud Rise by at least 0.06 psu (Methods section 'Salinity fluxes from upwelling'), which reduced upper-ocean stability[41] and preconditioned the 2016 opening. Spin-up of the barotropic Weddell gyre circulation due to strengthened wind stress curl (see Methods section 'Weddell Low') may have also enhanced topography- or eddy-related upwelling[29,31] and possibly topographic mixing as faster flow impinged on Maud Rise. Either could have intensified upward heat fluxes in 2016, contributing to the delayed freeze and presumably thinner ice in July. Ultimately, these upwelling- and storm-induced offshore polynyas are linked to positive fluctuations in SAM, which represent large-scale anomalies in the climate of the Southern Hemisphere.

The exceptional 1974–1976 Weddell polynyas, which were larger than the 2016–2017 openings (Fig. 1a), do not conform perfectly to this explanation. The 1974 event occurred under similar circumstances to the 2017 polynya, in that it was preceded by a positive deviation in SAM (Fig. 5b) and lower mean sea-level pressure (Fig. 5c), as well as delayed ice formation in 1973 (not shown) and a brief 'precursor' polynya that year[2,23] (Fig. 5a). But these anomalies were modest. The degree and spatial extent of preconditioning in 1974 were probably augmented by previously proposed mechanisms: a generally saltier Southern Ocean surface[19] and below-average precipitation over the preceding decade associated with prolonged negative SAM[47]. Reduced precipitation, however, cannot explain the 2016 opening, which followed six years of higher-than-average precipitation (Extended Data Fig. 9c).

Comparison with climate models

Accurate modelling of the Southern Ocean requires realistic simulation of deep water formation and ventilation processes[20]. This remains an urgent challenge. In many climate models that are included in the fifth Coupled Model Intercomparison Project (CMIP5), large Weddell polynyas featuring open-ocean deep convection recur on widely varying timescales[8,19]. In these models and others, heat steadily accumulates in Weddell Deep Water over several years or decades[5,10,22,48], possibly owing to freshwater forcing biases and insufficient vertical mixing[7,21]. This build-up eventually erodes stratification in an episode of spontaneous ventilation; cycles of recharge and discharge of heat then follow, associated with Weddell polynyas[5,8,10,22,48]. Observational records of ocean and sea ice are insufficiently long to assess whether these convective cycles, which create a global mode of internal variability[5,8–10,12,15], are natural or spurious. This is concerning, because some models suggest that recent Southern Ocean sea surface temperature and sea ice trends may simply reflect this cycle—that is, represent a rebound from ventilation during the 1974–1976 Weddell polynyas[10].

The 2016–2017 events offer an opportunity to assess whether destratification from mid-depth heat accumulation, which is prevalent in models, contributes to polynya formation in reality. The preceding decade-long hiatus in polynya activity is presumably long enough to discern trends in subsurface heat (Fig. 5a). However, we do not find marked heat accumulation before 2016 in records compiled from about 3,000 sub-pycnocline temperature measurements within the eastern Weddell region (Extended Data Fig. 9d, e, Extended Data Table 1; Methods section 'Sub-pycnocline temperature records'). Although the presence of warm Weddell Deep Water is required to sustain overturning, an increase in local heat content is probably not the immediate cause of polynyas near Maud Rise. This suggests that model results involving Weddell polynyas should be interpreted with greater caution, even when the simulated features resemble observed polynyas in size and location.

Similarly, although deep convection in simulated Weddell polynyas often proceeds until the subsurface heat reservoir is depleted[5,8,10,48], the observed cooling after the 1974–1976 and 2016–2017 polynyas of up to 1.0 °C (ref. [1]; see Methods section 'Sub-pycnocline temperature records') and 0.3 °C (Fig. 4a), respectively, is probably not severe enough to explain the lack of major openings in 1977[24] and 2018 (Fig. 5a). Instead, reductions in upwelling (Fig. 5e) and storm frequency (Fig. 5d), combined with westward advection of upper-ocean salinity anomalies away from Maud Rise[2,32], probably terminate multiyear polynya sequences.

Future implications

Progress in simulating and predicting offshore Antarctic polynyas will require a more precise understanding of how storms cause sea ice destruction and how upwelling affects haline stratification. New insight into these relationships may also inform long-standing questions on how Southern Ocean stratification modulates deep ventilation on glacial–interglacial timescales[49]; here, the possible role of offshore polynyas is poorly understood[16,17]. Although observations of additional offshore polynyas would be valuable in clarifying these mechanisms, climate models predict that their formation may soon be prohibited by the Southern Ocean surface freshening trend of about 0.01 psu per decade, which is associated with anthropogenic climate change[19]. However, this simulated non-convective regime has evidently not yet been reached. At present, we observe that the Maud Rise region experiences interannual variability in upper-ocean salinity—and thus also stability—that is an order of magnitude higher than this slow decadal freshening rate. This may enable intermittent openings similar to those in 2016 and 2017 for decades to come. Moreover, we identify statistically significant positive multidecadal trends in polynya-favourable conditions: the strengthening of SAM, Weddell Low, cyclonic wind stress curl and winter storm activity (Extended Data Table 1). These reflect poleward shifts in Southern Hemisphere westerly winds and storm tracks, which are expected to continue under anthropogenic forcing[44,50]. We propose that these changes may bring enhanced upwelling and a more frequently disturbed sea ice cover to the Weddell Sea region, conceivably signalling a greater future role for transient offshore polynyas in opening a window to the abyssal ocean.

Online content

Any methods, additional references, Nature Research reporting summaries, source data, extended data, supplementary information, acknowledgements, peer review information; details of author contributions and competing interests; and statements of data and code availability are available at https://doi.org/10.1038/s41586-019-1294-0.

Received: 14 January 2019; Accepted: 2 May 2019;
Published online: 10 June 2019

1. Gordon, A. L. Deep Antarctic convection west of Maud Rise. *J. Phys. Oceanogr.* **8**, 600–612 (1978).
2. Martinson, D. G., Killworth, P. D. & Gordon, A. L. A convective model for the Weddell Polynya. *J. Phys. Oceanogr.* **11**, 466–488 (1981).
3. Martinson, D. G. Evolution of the Southern Ocean winter mixed layer and sea ice: Open ocean deepwater formation and ventilation. *J. Geophys. Res.* **95**, 11641–11654 (1990).
4. Zanowski, H., Hallberg, R. & Sarmiento, J. L. Abyssal ocean warming and salinification after Weddell polynyas in the GFDL CM2G coupled climate model. *J. Phys. Oceanogr.* **45**, 2755–2772 (2015).
5. Martin, T., Park, W. & Latif, M. Multi-centennial variability controlled by Southern Ocean convection in the Kiel Climate Model. *Clim. Dyn.* **40**, 2005–2022 (2013).
6. Cheon, W. G., Park, Y.-G., Toggweiler, J. R. & Lee, S.-K. The relationship of Weddell Polynya and open-ocean deep convection to the Southern Hemisphere westerlies. *J. Phys. Oceanogr.* **44**, 694–713 (2014).
7. Heuzé, C., Ridley, J. K., Calvert, D., Stevens, D. P. & Heywood, K. J. Increasing vertical mixing to reduce Southern Ocean deep convection in NEMO3.4. *Geosci. Model Dev.* **8**, 3119–3130 (2015).
8. Behrens, E. et al. Southern Ocean deep convection in global climate models: A driver for variability of subpolar gyres and Drake Passage transport on decadal timescales. *J. Geophys. Res. Oceans* **121**, 3905–3925 (2016).
9. Pedro, J. B. et al. Southern Ocean deep convection as a driver of Antarctic warming events. *Geophys. Res. Lett.* **43**, 2192–2199 (2016).
10. Zhang, L., Delworth, T. L., Cooke, W. & Yang, X. Natural variability of Southern Ocean convection as a driver of observed climate trends. *Nat. Clim. Change* **9**, 59–65 (2019).
11. Bernardello, R., Marinov, I., Palter, J. B., Galbraith, E. D. & Sarmiento, J. L. Impact of Weddell Sea deep convection on natural and anthropogenic carbon in a climate model. *Geophys. Res. Lett.* **41**, 7262–7269 (2014).

12. Resplandy, L., Séférian, R. & Bopp, L. Natural variability of CO_2 and O_2 fluxes: what can we learn from centuries-long climate models simulations? *J. Geophys. Res. Oceans* **120**, 384–404 (2015).
13. Moore, G. W. K., Alverson, K. & Renfrew, I. A. A reconstruction of the air–sea interaction associated with the Weddell polynya. *J. Phys. Oceanogr.* **32**, 1685–1698 (2002).
14. Weijer, W. et al. Local atmospheric response to an open-ocean polynya in a high-resolution climate model. *J. Clim.* **30**, 1629–1641 (2017).
15. Cabré, A., Marinov, I. & Gnanadesikan, A. Global atmospheric teleconnections and multidecadal climate oscillations driven by Southern Ocean convection. *J. Clim.* **30**, 8107–8126 (2017).
16. Amblas, D. & Dowdeswell, J. A. Physiographic influences on dense shelf-water cascading down the Antarctic continental slope. *Earth Sci. Rev.* **185**, 887–900 (2018).
17. Smith, J. A., Hillenbrand, C.-D., Pudsey, C. J., Allen, C. S. & Graham, A. G. C. The presence of polynyas in the Weddell Sea during the Last Glacial Period with implications for the reconstruction of sea-ice limits and ice sheet history. *Earth Planet. Sci. Lett.* **296**, 287–298 (2010).
18. Broecker, W. S., Sutherland, S. & Peng, T.-H. A possible 20th-century slowdown of Southern Ocean deep water formation. *Science* **286**, 1132–1135 (1999).
19. de Lavergne, C., Palter, J. B., Galbraith, E. D., Bernardello, R. & Marinov, I. Cessation of deep convection in the open Southern Ocean under anthropogenic climate change. *Nat. Clim. Change* **4**, 278–282 (2014).
20. Heuzé, C., Heywood, K. J., Stevens, D. P. & Ridley, J. K. Southern Ocean bottom water characteristics in CMIP5 models. *Geophys. Res. Lett.* **40**, 1409–1414 (2013).
21. Kjellsson, J. et al. Model sensitivity of the Weddell and Ross seas, Antarctica, to vertical mixing and freshwater forcing. *Ocean Model.* **94**, 141–152 (2015).
22. Reintges, A., Martin, T., Latif, M. & Park, W. Physical controls of Southern Ocean deep-convection variability in CMIP5 models and the Kiel Climate Model. *Geophys. Res. Lett.* **44**, 6951–6958 (2017).
23. Comiso, J. C. & Gordon, A. L. Recurring polynyas over the Cosmonaut Sea and the Maud Rise. *J. Geophys. Res.* **92**, 2819–2833 (1987).
24. Carsey, F. D. Microwave observation of the Weddell polynya. *Mon. Weath. Rev.* **108**, 2032–2044 (1980).
25. Lindsay, R. W., Holland, D. M. & Woodgate, R. A. Halo of low ice concentration observed over the Maud Rise seamount. *Geophys. Res. Lett.* **31**, L13302 (2004).
26. Swart, S. et al. Return of the Maud Rise polynya: climate litmus or sea ice anomaly? [in "State of the Climate in 2017"]. *Bull. Am. Meteorol. Soc.* **99**, S188–S189 (2018).
27. Wang, G. et al. Compounding tropical and stratospheric forcing of the record low Antarctic sea-ice in 2016. *Nat. Commun.* **10**, 13 (2019).
28. Meehl, G. A. et al. Sustained ocean changes contributed to sudden Antarctic sea ice retreat in late 2016. *Nat. Commun.* **10**, 14 (2019).
29. Gordon, A. L. & Huber, B. A. Southern Ocean winter mixed layer. *J. Geophys. Res.* **95**, 11655–11672 (1990).
30. Holland, D. M. Explaining the Weddell Polynya—a large ocean eddy shed at Maud Rise. *Science* **292**, 1697–1700 (2001).
31. de Steur, L., Holland, D. M., Muench, R. D. & McPhee, M. G. The warm-water "Halo" around Maud Rise: properties, dynamics and impact. *Deep Sea Res. Part I* **54**, 871–896 (2007).
32. Kurtakoti, P., Veneziani, M., Stössel, A. & Weijer, W. Preconditioning and formation of Maud Rise polynyas in a high-resolution earth system model. *J. Clim.* **31**, 9659–9678 (2018).
33. Wilson, E. A., Riser, S. C., Campbell, E. C. & Wong, A. P. S. Winter upper-ocean stability and ice–ocean feedbacks in the sea ice-covered Southern Ocean. *J. Phys. Oceanogr.* **49**, 1099–1117 (2019).
34. Martinson, D. G. & Iannuzzi, R. A. in *Antarctic Sea Ice: Physical Processes, Interactions and Variability (Antarctic Research Series)* Vol. 74 (ed. Jeffries, M. O.) 243–271 (American Geophysical Union, 1998).
35. Timmermann, R., Lemke, P. & Kottmeier, C. Formation and maintenance of a polynya in the Weddell Sea. *J. Phys. Oceanogr.* **29**, 1251–1264 (1999).
36. McPhee, M. G. Marginal thermobaric stability in the ice-covered upper ocean over Maud Rise. *J. Phys. Oceanogr.* **30**, 2710–2722 (2000).
37. Itkin, P. et al. Thin ice and storms: sea ice deformation from buoy arrays deployed during N-ICE2015. *J. Geophys. Res. Oceans* **122**, 4661–4674 (2017).
38. McPhee, M. G. et al. The Antarctic Zone Flux Experiment. *Bull. Am. Meteorol. Soc.* **77**, 1221–1232 (1996).
39. Våge, K. et al. Surprising return of deep convection to the subpolar North Atlantic Ocean in winter 2007–2008. *Nat. Geosci.* **2**, 67–72 (2009).
40. Testor, P. et al. Multiscale observations of deep convection in the northwestern Mediterranean Sea during winter 2012–2013 using multiple platforms. *J. Geophys. Res. Oceans* **123**, 1745–1776 (2018).
41. Motoi, T., Ono, N. & Wakatsuchi, M. A mechanism for the formation of the Weddell Polynya in 1974. *J. Phys. Oceanogr.* **17**, 2241–2247 (1987).
42. Mantyla, A. W. & Reid, J. L. Abyssal characteristics of the World Ocean waters. *Deep-Sea Res. A* **30**, 805–833 (1983).
43. Jullion, L. et al. The contribution of the Weddell Gyre to the lower limb of the Global Overturning Circulation. *J. Geophys. Res. Oceans* **119**, 3357–3377 (2014).
44. Thompson, D. W. J. et al. Signatures of the Antarctic ozone hole in Southern Hemisphere surface climate change. *Nat. Geosci.* **4**, 741–749 (2011).
45. Fogt, R. L., Wovrosh, A. J., Langen, R. A. & Simmonds, I. The characteristic variability and connection to the underlying synoptic activity of the Amundsen-Bellingshausen Seas Low. *J. Geophys. Res. Atmos.* **117**, D07111 (2012).
46. Cheon, W. G. et al. Replicating the 1970s' Weddell Polynya using a coupled ocean-sea ice model with reanalysis surface flux fields. *Geophys. Res. Lett.* **42**, 5411–5418 (2015).
47. Gordon, A. L., Visbeck, M. & Comiso, J. C. A possible link between the Weddell Polynya and the Southern Annular Mode. *J. Clim.* **20**, 2558–2571 (2007).
48. Dufour, C. O. et al. Preconditioning of the Weddell Sea polynya by the ocean mesoscale and dense water overflows. *J. Clim.* **30**, 7719–7737 (2017).
49. Sigman, D. M., Hain, M. P. & Haug, G. H. The polar ocean and glacial cycles in atmospheric CO_2 concentration. *Nature* **466**, 47–55 (2010).
50. Chang, E. K. M., Guo, Y. & Xia, X. CMIP5 multimodel ensemble projection of storm track change under global warming. *J. Geophys. Res. Atmos.* **117**, D23118 (2012).

METHODS

Regions. Various gridded fields were averaged within the Maud Rise region (63°–67° S, 0°–10° E), which loosely encompasses the 4,000 m isobath around the seamount (Fig. 1b, c) and the area of polynya formation in 2016 and 2017. Other metrics were calculated within an area that we designate the eastern Weddell region (62°–68° S, 15° W–20° E), which spans the eastern Weddell, Lazarev and western Riiser-Larsen seas. This larger area increases signal strength for records with spatial uncertainty or sparsity, such as discrete polynya events, storm statistics and precipitation.

In the context of hydrographic observations, the Maud Rise region instead refers to a radius of 250 km from Maud Rise (65° S, 3° E; see Extended Data Fig. 1). This encloses the 'halo' of elevated subsurface heat content identified over the seamount[31,51]. Here the eastern Weddell region refers to hydrographic observations collected within 500 km of Maud Rise.

Sea ice concentration data. Satellite observations of Antarctic sea ice before 1972 are presently limited to a visible-band composite of September 1964 from the NASA Nimbus I mission, which showed a possible offshore polynya in the Weddell Sea[52]. The quality of the imagery prevents conclusive identification. The modern passive microwave SIC era began in 1972 with the single-channel Nimbus-5 Electrically Scanning Microwave Radiometer (ESMR)[24]. We use daily SIC from December 1972 to May 1977 from the NSIDC Nimbus-5 ESMR v1 product on a 25-km polar stereographic grid, the result of heavy reprocessing[53]. Gaps of weeks to months are present.

A series of more reliable multi-channel sensors followed. We use the merged NASA Goddard Space Flight Center v3 25-km product distributed by NSIDC from November 1978 to December 2017[54]. The merged Goddard product is nearly identical to the NOAA/NSIDC Climate Data Record (CDR), which is based on two well-validated SIC algorithms, with two main differences: additional manual quality control and inclusion of the period from 1978–1987, for which SIC data are available every other day[54,55]. From January 2018 to February 2019, we use the NOAA/NSIDC Near-Real-Time (NRT) CDR v1 product[56]. The combined 'NSIDC Merged' record from 1978–2019 was used for SIC climatology (Fig. 2a) and polynya identification (Fig. 5a). Nimbus-5 ESMR was included in the polynya record to highlight the 1974–1976 events, although precise quantitative comparison with NSIDC Merged is not possible. For more qualitative analyses, we use higher-resolution daily SIC data from the Advanced Microwave Scanning Radiometer (AMSR) sensors (see Fig. 2a for comparison with NSIDC Merged). We use the University of Bremen v5 AMSR-E (2002–2011) and AMSR2 (2012–2019) products, derived using the ARTIST Sea Ice (ASI) algorithm at a resolution of 6.25 km[57,58].

SIC climatology (Fig. 2a) includes days with valid data from at least 75% of grid cells in the Maud Rise region. Median and 25%–75% IQR time series were generated by compositing over day-of-year, then filtering with a 7-day centred running mean. Along-trajectory SIC (Fig. 4) represents the average SIC from AMSR2-ASI (from 4 July 2012 onwards) or NSIDC Merged (from 19 December 2011 to 3 July 2012) within a moving 1° latitude × 2° longitude box centred on the given or estimated location for each float profile.

Polynya identification. A polynya is defined as any nonlinear-shaped opening within sea ice that contains open water, brash ice, new ice, nilas and/or young ice[59]. Passive microwave sensing generally underestimates SIC for new, thin ice, aiding the detection of polynyas[60,61]. Following past studies identifying polynyas in the Cosmonaut Sea[62,63], we define 'polynya extent' as the sum of connected pixels (allowing diagonal connections) with SIC beneath some threshold. We excluded areas connected to the open ocean (that is, embayments), common during transitional freeze and melt periods, and calculated the centroid of individual openings. Patches of ice within connected open regions were negated using a binary dilation algorithm to ensure that polynya extent, rather than area, was quantified.

Figure 5a highlights midwinter openings that appear from closed ice cover, as occurred in 2016 and 2017 (Extended Data Figs. 2, 8). These differ from early-winter embayments that later became enclosed, such as occurred in 1974 (ref. [24]). The latter probably reflects ocean preconditioning strong enough to permit overturning from slight amounts of ice growth or even cooling alone (a 'thermal mode' of stratification)[2,35,41,64]. This mode does not require perturbations such as storms, which we identify as critical for midwinter openings. For comparison, we included the 1974–1976 polynyas in our record despite their different mode of formation.

We consider the period of closed ice cover over Maud Rise to be delimited each winter by one week after the first date of 90% average SIC and one week before the last date of 90% SIC, consistent with climatological SIC[25]. The one-week buffers account for gradual ice advance and retreat, during which small, brief openings frequently form via enclosure and climatological melt[23]. Fixed start and/or end dates of 1 July and 31 October, consistent with climatology (Fig. 2a), were used for freeze and/or melt seasons with already-established polynyas (1974–1976, 2017) or some gaps in SIC data (1973). Other winters with major data gaps (1972, 1977, 1978, 1987) were omitted from the record. The summed daily extent of polynyas with centroids in the eastern Weddell region was calculated using SIC thresholds of 40%, 50% and 60% for comparison, because grid connectivity is sensitive to SIC threshold. These thresholds reflect the dynamic mix of open water and new ice within polynyas[61], and lie between the low (for example, 15%) thresholds used to define the seasonal ice edge and high (for example, 80%) thresholds previously used to identify Antarctic offshore polynyas[62,63]. Dates with non-zero total polynya extent at the 60% threshold, chosen to maximally differentiate years from one another, were designated 'polynya days'. As an approximation, polynya day counts from 1979–1986 were doubled because SIC data are available every other day. Our average SIC threshold of 50% was used in Fig. 1a, which depicts the largest polynya identified within the Maud Rise region on each date, and Figs. 2a, 3a, which track the summed extent of polynyas with centroids in the eastern Weddell region.

The accuracy of our methodology was checked by visually inspecting SIC images. Our assessment is consistent with previous reports of Maud Rise polynyas in 1973[2,23], 1980[23], 1994[30,51,65] and 2005[31]. A previous analysis for the Maud Rise region of total days with average SIC under 92% from 1979–2004[47] is qualitatively similar to our polynya record. Given the association of deep convection with coherent openings[1], however, we focus on discrete polynya events, rather than slight reductions in SIC. We note that a small opening outside the detection parameters of our algorithm (and therefore absent in Fig. 5a) appeared above Maud Rise in late October 2018, just before climatological melt.

Hydrographic data. Argo profiling floats drift at a depth of around 1,000 m and sample every 7–10 days, profiling on ascent[66]. Sampling intervals are generally 2 dbar above 1,000 m and 100 dbar below 1,000 m (ref. [67]). Measurements are rated to accuracies of at least 0.005 °C, 0.01 psu and 2.5 dbar (ref. [66]). An ice-avoidance algorithm monitors median temperature between 50 and 20 m, aborting ascent if near the freezing point, which indicates ice cover[67–69]. Under-ice profiles are stored without position fixes and transmitted upon spring ice melt. A rare exception is when a float surfaces within a polynya, as occurred in 2017 with SOCCOM floats 5904468 and 5904471 (Extended Data Fig. 8). Because the algorithm requires three consecutive ice-free determinations[67], both floats inferred warm conditions in or near the polynya over about 21 days before surfacing.

All Argo temperature and salinity measurements (Extended Data Fig. 1) south of 55° S and between 70° W and 50° E through 1 October 2018 were downloaded from the US-GODAE Global Data Assembly Center (GDAC)[70]. We rejected profiles without timestamps, consecutive under-ice profiles with timestamps erroneously reflecting transmission upon ice melt, and data from floats affected by position and date jumps and other quality control issues.

Under-ice or missing positions (quality control flags '8' or '9') were linearly interpolated, using profile timestamps to assign distances along great circle routes between known GPS fixes. Advanced methods, such as interpolation along contours of planetary potential vorticity, could reduce position uncertainty over some areas of the Weddell Sea; however, this may not be the case near Maud Rise, particularly to the southwest and northeast of the seamount[71]. Given the tendency of floats to remain trapped over Maud Rise (Fig. 1b, c) owing to Taylor column dynamics[31,51,72], it is unlikely that floats 5903616, 5904468 and 5904471 deviated away from the seamount during the winters of 2012 through to 2017. SOCCOM float deployments were conducted with this phenomenon in mind[73].

Both real-time ('R') and delayed-mode ('D') data were obtained. Although both have passed automatic quality control checks, only delayed-mode data have undergone detailed quality control inspection, although sensor drift calibrations often extend automatically to real-time profiles[70]. If a profile was available on delayed-mode, we used its adjusted parameters. The first cast within a profile file was selected if multiple were available. Only depths at which all three quality control flags for pressure, temperature, and salinity were good ('1') or probably good ('2') were extracted.

Float 5904468 represents an exception to this procedure. Drift in its salinity sensor, a Sea-Bird SBE-41CP conductivity cell, began in early 2016 at a rate of approximately 0.07 psu per year, constant with depth and linear in time. This drift was corrected through 13 May 2017 (profile 83) by the GDAC using standard procedures (weighted least-squares fit to deep climatology based on nearby Argo data). We extended this correction from 23 May 2017 (profile 84) to 8 May 2018 (profile 118) by subtracting the linear trend of 1,600–1,700 m average salinity, calculated from profiles linearly interpolated to 1-m spacing. Corrected 1,600–1,700 m average salinity agrees with that measured by the nearby float 5904471 over 2015–2018 (see Fig. 1b, c) to within about 0.01 psu except for periods of mixing during the 2017 polynya. Profiles from 119 onwards were not used.

Salinity measurements are provided by the GDAC with a precision of 0.001 psu. The combination of weak vertical salinity gradient in the Weddell Sea and fine sampling interval (2 dbar) creates artificial 0.001 psu steps, generating spurious static instabilities. We applied a mild quadratic smoothing spline (*UnivariateSpline* from SciPy with smoothing factor $s = 0.00015$) to all float salinity profiles, attenuating these jumps while preserving integrity of the profile. This procedure essentially downsamples the salinity measurements to allow buoyancy frequency to be accurately resolved at all depths.

Dissolved oxygen measurements from floats 5904468 and 5904471 were downloaded from the SOCCOM quality-controlled archive[74]. Dissolved oxygen data from the non-SOCCOM float 5903616 were obtained from the University of Washington (UW) Calibrated O_2 package, v1.1[75], with updated profiles provided by R. Drucker (personal communication). The sampling interval of dissolved oxygen is coarser than for CTD data, ranging from about 5 dbar above 100 m to about 100 dbar below 1,000 m[67]. Dissolved oxygen optodes onboard most SOCCOM floats collect in-air samples for direct calibration, allowing for accuracy of about 1% of near-surface values (around 325 μmol kg^{-1}), or 3 μmol kg^{-1} (ref. [76]). The optode on 5903616 lacks this capability and instead has been calibrated to deep reference data, with an accuracy of about 2%, or 7 μmol kg^{-1} (ref. [75]). Comparison of UW-calibrated dissolved oxygen from 5903616 with SOCCOM-calibrated dissolved oxygen from 5904468 and 5904471—performed in surface-referenced potential density space—revealed a positive bias of about 6.0 μmol kg^{-1}, uniform in depth, during their overlap period at Maud Rise (2015–2016). We subtracted this offset from all UW-O_2 profiles by float 5903616.

Shipboard CTD and bottle data and instrumented elephant seal profiles (Extended Data Fig. 1) featuring both temperature and salinity were obtained at original depth levels from the World Ocean Database 2018 prerelease[77] with August 2018 additions. Depth levels were retained only if global quality control flags for depth, temperature and salinity profiles as well as the three quality control flags at that depth were marked good ('0').

Instrumented elephant seals typically dive to about 600 m while foraging, although dives to 2,000 m occasionally occur[78]. CTD measurements begin at the deepest point of a dive and continue during ascent; data may be collected on as many as four dives per day[79]. Owing to data transfer and energy constraints, casts are transmitted in compressed form. A 'broken-stick' algorithm selects 10–25 depths that best represent the profile; thus, resolution may be coarse for deeper profiles[78,79]. The filters we apply when creating hydrographic climatologies account for this possibility (see below). Measurement accuracy is estimated at 0.04 °C and 0.03 psu[80], lower than for floats; satellite fixes are accurate to about 5 km (ref. [78]).

Derived oceanographic quantities. The Python implementation of the Gibbs SeaWater Oceanographic Toolbox of TEOS-10 (https://teos-10.github.io/GSW-Python/) was used to compute profiles of depth or pressure, potential temperature, surface-referenced potential density, and buoyancy (Brunt-Väisälä) frequency squared (N^2). We interpolated N^2 profiles to 1-m spacing, then applied a 50-m centred running mean. This filtering reduces noise and spikes, allowing patches of consistently low N^2 to be visible in Fig. 4d and Extended Data Fig. 6d despite the compressed vertical axis.

Mixed-layer depths (MLD; Fig. 4, Extended Data Figs. 3c, 6) were determined as the depth at which surface-referenced potential density exceeds its value at $z_{ref} = 10$ m, estimated using interpolation or nearest-neighbour extrapolation, by a threshold of $\Delta\sigma_\theta = 0.03$ kg m^{-3} (refs [81,82]). Mixed-layer temperature (MLT) and mixed-layer salinity (MLS) were averaged from profiles interpolated to 0.1-m spacing and extrapolated to the surface. We note that MLDs sometimes shoaled sharply during the 2016 and 2017 polynyas, rather than deepening (Extended Data Fig. 3c). This reflects the development of shallow fresh layers from ice melt (Fig. 2b), as seen in idealized ice–ocean model experiments with storm perturbations[33]. The two profiling floats, sampling coarsely in time and space, did not observe active overturning, which probably occurred within plumes of horizontal scale $O(100$ m) occupying a fraction of the convection region[40,83,84] at locations with a weaker melt layer or pycnocline. The observed interior mixed layers (Extended Data Fig. 6) may have been formed by nearby deep convection, communicated laterally through efficient mixing due to baroclinic instability.

Upper-ocean freshwater anomaly (Extended Data Fig. 3e), or 'salt deficit'[3,33,34], was integrated from 0–250 m, encompassing MLDs in all seasons (see Extended Data Fig. 3c) and salinity variability an order of magnitude greater than below 250 m. The metric was computed as in ref. [33], in terms of the freshwater provided by melt of an equivalent sea ice thickness (units of metres):

$$\eta(250\,\mathrm{m}) = \frac{1}{\Delta S_i}\int_{0\,\mathrm{m}}^{250\,\mathrm{m}} [S(250\,\mathrm{m}) - S(z)]\,\mathrm{d}z$$

where S is salinity and ΔS_i is the approximate salinity difference between ocean and sea ice (about 30 psu)[34]. Trapezoidal integration was applied to profiles interpolated and extrapolated as above.

To interpret the climatological 0–250 m freshwater anomaly (grey shading in Extended Data Fig. 3e), we assume that brine rejection approximately balances ice melt from local and nonlocal sources, because Maud Rise is near the circumpolar line of zero annual net freshwater flux associated with sea ice[85], and that salt fluxes from geostrophic advection are relatively small. This implies that positive salt fluxes from Ekman upwelling (due to cyclonic wind stress curl; see Fig. 5e) approximately balance precipitation and evaporation on an annual net basis. We thus interpret the seasonal cycle of climatological 0–250 m freshwater anomaly as predominantly reflecting brine rejection and ice melt. A similar approach has been used to estimate ice formation rates from instrumented seal profiles offshore of East Antarctica[86].

Convection resistance (CR) represents the buoyancy loss required for overturning to reach a given depth, H:

$$\mathrm{CR}(H) = \frac{g}{\rho_0}\int_{0\,\mathrm{m}}^{H} [\sigma_\theta(H) - \sigma_\theta(z)]\,\mathrm{d}z$$

where g is acceleration due to gravity, ρ_0 is a seawater reference density (1,027.8 kg m^{-3}), and σ_θ is surface-referenced potential density[19,87,88]. Depth sections of convection resistance illustrate that low interior stratification combined with a weakened winter halocline, as occurred in 2016 and 2017, may permit deep-reaching convection near Maud Rise (Extended Data Fig. 6e).

Composites of float time series. Data from floats 5903616 (active only until 2 June 2016), 5904468 and 5904471 were combined to create time series of MLS, MLD, MLT and 0–250 m freshwater anomaly in 2016 and 2017 (Fig. 2b, Extended Data Fig. 3c–e). Float measurements were linearly interpolated to daily resolution, and the daily means (for MLT and MLD), maxima (for MLS), or minima (for freshwater anomaly) were calculated. MLS and MLT agree between the three floats to within 0.05 psu and 0.25 °C, except in the 2–3 months after ice melt. Freshwater anomaly and MLD are more variable, but fluctuations generally occur synchronously. Maximum MLS and minimum freshwater anomaly were chosen to highlight the most extreme preconditioning observed near Maud Rise, motivated by the notion that overturning will preferentially occur where stratification is weakest. Given the substantial spatial inhomogeneity around Maud Rise[31,32], sampling by 2–3 floats probably underestimates the most extreme preconditioning that occurred in 2016–2017.

The red line in Fig. 2b represents the MLS required to eliminate stratification between the mixed layer and 250 m, at which point initiation of deep convection would be trivial[3]. This 'overturning limit' is fresher than salinity at 250 m owing to the destabilizing warmth of the thermocline[33]. Its value was determined as the MLS at which surface density, computed using composite (average) MLT, would exceed composite surface-referenced potential density at 250 m. The use of surface density neglects the development of thermobaric instabilities, which could hasten overturning near this limit of zero stratification[36].

Salinity fluxes from upwelling. Upwelling due to divergence of Ekman transport can cause heat and salt fluxes into the mixed layer[28,35,89]. Vertical velocity w_{Ek} at the base of the Ekman layer is related to wind stress curl[90] in the absence of ice cover:

$$w_{\mathrm{Ek}} = \nabla\cdot\boldsymbol{U}_{\mathrm{Ek}} = \boldsymbol{k}\cdot\nabla\times\frac{\boldsymbol{\tau}}{\rho_0 f}$$

where $\boldsymbol{U}_{Ek}$ is the horizontal vector Ekman transport, $\boldsymbol{k}$ is the vertical unit vector, $\boldsymbol{\tau}$ is the vector surface wind stress, ρ_0 is a seawater reference density (1,027.8 kg m^{-3}), and f is the Coriolis parameter.

Upwelling prevails over Maud Rise because wind stress curl is consistently negative (Fig. 5e). We estimated, in back-of-the-envelope fashion, the anomalous mixed-layer salt flux resulting from record cyclonic wind stress curl over Maud Rise in the ice-free months of 2015 and 2016—before the 2016 polynya—compared to a typical previous year (Fig. 5e; Methods section 'Atmospheric reanalysis'). The average wind stress curl from ERA-I over 1979–2014 was -2.06×10^{-7} N m^{-3}, whereas the averages for January–May 2015 and 2016 were -2.90×10^{-7} N m^{-3} and -3.08×10^{-7} N m^{-3}, respectively, increasing upwelling by 8.0 m and 9.8 m.

To estimate the corresponding mixed-layer salt flux, salinity gradients across the base of the mixed layer were measured using observations from floats 5903616, 5904468 and 5904471 over January–May 2015 and 2016. MLD during these periods averaged 41.3 m and 56.2 m, respectively. MLS averaged 33.90 psu and 34.22 psu, while the average salinities of depth levels between the time-varying MLD and 7.8 m or 9.6 m below the MLD were 34.09 psu and 34.34 psu, respectively. Expected MLS elevation was computed using these values:

$$\Delta S_{\mathrm{ml}} = \frac{h_{\mathrm{up}}S_{\mathrm{up}} + (h_{\mathrm{ml}} - h_{\mathrm{up}})S_{\mathrm{ml}}}{h_{\mathrm{ml}}} - S_{\mathrm{ml}}$$

where S_{ml} and S_{up} are MLS and sub-mixed-layer salinity, and h_{ml} and h_{up} represent MLD and thickness of the upwelled layer. We determine that additional Ekman upwelling elevated MLS by at least 0.04 psu in 2015 and 0.02 psu in 2016, for a total of at least 0.06 psu. These are lower bounds because upwelling continues in winter, although the absence of ice–ocean stress data precludes the estimation of upwelling during ice-covered months. Statistically propagating the Argo salinity measurement accuracy of ±0.01 psu yields a ΔS_{ml} uncertainty of just ±0.002 psu; however, additional contributions from the exclusion of ice-covered months,

coarseness of sampling, spatial inhomogeneity and time averaging are less easily quantified.

Hydrographic climatologies. Float, shipboard and instrumented seal measurements were used to create climatologies of average MLS, MLD, MLT and 0–250 m freshwater anomaly near Maud Rise ($R < 250$ km) and away from Maud Rise (250 km $< R <$ 500 km; Fig. 2b, Extended Data Fig. 3c–e). Profiles with a shallowest measurement below 30 m, deepest measurement above 250 m, or MLD greater than 250 m were excluded, ensuring that the mixed layer and upper seasonal pycnocline were captured. These filters yielded 1,035 float profiles from 50 floats, 265 shipboard casts, and 124 seal profiles near Maud Rise, and 1,523 float profiles from 79 floats, 510 shipboard casts, and 445 seal profiles away from Maud Rise (Extended Data Fig. 1). Mean and median years of the compiled observations are 2008 and 2012 for Maud Rise and 2006 and 2008 away from Maud Rise. Fewer than 1% of these observations were collected before 1970.

Calculated metrics were composited by day-of-year within 365 overlapping 21-day bins, looping from December to January. Median and 25%–75% IQR were computed for each bin instead of mean and standard deviation to reduce sensitivity to outliers and reflect skewness in spatial and temporal variability. Lastly, a 21-day centred running mean was applied. We note that the absence of abrupt changes in these metrics—for example, sharp increases in MLS during ice formation—is an artefact of the compositing method. Years featuring early and late ice formation are combined, for example, resulting in gradual changes.

Sub-pycnocline temperature records. Extended Data Fig. 9d, e depicts 15.5 years (2002–2017) of 258-m temperature anomalies from climatology within the eastern Weddell region ($R < 500$ km from Maud Rise) based on 2,445 float, 151 shipboard and 407 seal profiles, and 250–1,000 m average temperature anomalies based on 2,421 float and 133 shipboard profiles and one seal profile. We compare observations with a gridded 1/4° monthly climatology, the 2018 WOCE/Argo Global Hydrographic Climatology[91] (WAGHC).

We included profiles with a shallowest measurement above 30 m and a deepest measurement below the depth(s) of interest. Temperatures at 258 m or at the 14 WAGHC levels from 218–1,050 m were estimated from each profile using linear interpolation. Observations were co-located in space with WAGHC fields using nearest-neighbour interpolation, then the climatological value on a given day-of-year was estimated using linear interpolation over values assigned to the 15th of each month. The average 250–1,000 m anomaly was computed after linearly interpolating anomalies at the 14 depths (218–1,050 m) to 1-m spacing. Lastly, the anomalies were binned biannually, with at least five samples required in each bin. Extended Data Fig. 9d, e displays median and 25%–75% IQR values in addition to violin plots, which represent a kernel density distribution of the binned data.

Decadal changes in Weddell gyre heat content are probably closely related to Circumpolar Deep Water inflow variability[92,93], but uncertainty remains regarding the importance of internal processes such as offshore polynyas[94,95]. Ventilation during the 1974–1976 openings cooled depths from 200–2,700 m by 0.4 °C within the polynya area[96], a signal that propagated into deep and abyssal waters away from the Weddell Sea through advective transport and wave mechanisms[4,97]. Nonetheless, local rebound in heat content near Maud Rise had occurred by 1984[94]. The absence of polynya activity in the latter half of the 1980s (Fig. 5a) is thus further evidence against a recurrence timescale governed exclusively by deep heat recharge.

Polynya heat flux estimates. Gradual deep cooling and freshening observed by both floats from 2015 to early 2016 (Extended Data Fig. 6a, b) probably reflects movement of floats from the warm 'halo' encircling Maud Rise into its overlying Taylor column regime (Fig. 1b). However, subsequent deep anomalies are inconsistent with hydrographic surveys conducted in 1994[51] and 2005[31], despite conditions coincidentally also favouring polynya formation in those years (Fig. 5a). We thus attribute these abrupt decreases in heat content primarily to ventilation during the 2016 polynya. We difference sub-mixed-layer potential temperature profiles for each float immediately before 27 July 2016 with those over the five succeeding months until 1 January 2017 to estimate the rate of convective heat loss (Q, in W m^{-2}):

$$Q = \frac{\rho_0 c_p}{\Delta t} \int_{1{,}650\,\mathrm{m}}^{200\,\mathrm{m}} \Delta\theta(z)\mathrm{d}z$$

where ρ_0 is a seawater reference density (1,027.8 kg m^{-3}), c_p is the specific heat of seawater (3,850 J kg^{-1} °C^{-1}), Δt is the polynya duration (21 days), and $\Delta\theta(z)$ is the change in potential temperature at depth z. The median heat flux is 208 W m^{-2} from 31 profiles, 74% of which yield estimates between 0 W m^{-2} and the average ocean–atmosphere turbulent heat flux during the polynya, 252 W m^{-2} (Fig. 3c, Extended Data Fig. 7). Estimates outside this range may reflect lateral mixing or float displacement.

Southern Annular Mode. In its positive phase, SAM is characterized by lower pressure over Antarctica than over mid-latitudes, associated with poleward displacement of the mid-latitude westerly jet[44]. We use a monthly index of SAM from 1972–2019[98]. The index is filtered using a two-year centred running mean in Fig. 5b to highlight lower-frequency fluctuations.

Atmospheric reanalysis. Six-hourly and monthly-mean 0.75°-resolution surface-level analysis and forecast fields from ERA-Interim (ERA-I), a third-generation global reanalysis product[99], were obtained from January 1979 to December 2018. Forecast output was de-accumulated, and climatologies were constructed by compositing over day-of-year, calculating mean and 25%–75% IQR values, and filtering using a seven-day centred running mean.

10-m wind speed (Fig. 3b, Extended Data Fig. 4) was calculated as:

$$|\boldsymbol{u}| = \sqrt{u^2 + v^2}$$

Wind stress curl (Fig. 5e) was computed using second-order-accurate central differencing:

$$\nabla \times \boldsymbol{\tau} = \frac{\Delta \tau_y}{\Delta x} - \frac{\Delta \tau_x}{\Delta y}$$

Given the uncertainty of ice motion products near ice–ocean boundaries and in areas of low SIC[100], we instead estimate wind-forced ice drift velocities (u_i and v_i) from ERA-I using a 'rule-of-thumb' for thin Weddell Sea pack ice that suggests drift is around 3% of wind speed at a turning angle of around 23° to the left of winds[101]. Others have used a scaling of 2% and turning angle of 30° (ref. [102]); our results are not sensitive to the choice of these parameters. Potential ice divergence due to wind forcing (Extended Data Fig. 5) was inferred from these drift velocities:

$$\nabla \cdot \boldsymbol{u}_i = \frac{\Delta u_i}{\Delta x} + \frac{\Delta v_i}{\Delta y}$$

Because geostrophic winds are nondivergent, the response of a spatially uniform ice cover will also be nondivergent despite the turning angle[103]. Ice divergence therefore requires deviations from geostrophy, such as sub-geostrophic speeds associated with gradient winds in an intense cyclone, or spatially inhomogeneous ice properties. Extended Data Fig. 5 highlights potential ice divergence associated with the former. Divergence during storm episodes probably also occurs owing to ice deformation on shorter spatial scales than those resolved by ERA-I[37].

Under weak winds, ocean heat loss within a polynya may warm the lower atmosphere enough to generate a persistent low-pressure anomaly, cyclonic wind field, and ice divergence, thus maintaining the opening[2,35]. This positive feedback is not apparent in ERA-I in 2016 (Extended Data Fig. 5) or 2017 (not shown), perhaps because anomalies are quickly advected downstream by background winds and transient storms.

Ocean-atmosphere turbulent heat fluxes were estimated from ERA-I fields using the COARE 2.0 bulk flux algorithm[104], as described in ref. [105]. Calculated open-water heat fluxes for each grid cell were scaled by open water fraction (1 − SIC) from ERA-I and averaged within the Maud Rise region. Dividing by the mean open water fraction yields the average heat flux within the 2016 polynya (Fig. 3c).

Weddell Low. We designate the Weddell Low as the climatological low mean sea-level pressure (MSLP) centre over the Riiser-Larsen Sea, around which a large-scale geostrophic wind field circulates[106]. The curl of this wind field has a leading role in controlling the strength of the Weddell gyre[107–109]. By analogy to the Amundsen Sea Low[45], the Weddell Low may be expected to modulate cyclone central pressures and spatial density across the Weddell Sea region. We characterize the Weddell Low as the region $\pm 1\sigma$ in latitude and longitude around the minimum ERA-I monthly mean MSLP identified within 60°–70° S, 60° W–60° E. The average minimum occurs at 64.4° S, 16.7° E, resulting in an area bounded by 61.9°–66.8° S, 12.5° W–45.8° E. The Weddell Low index represents monthly mean MSLP within this region, filtered using a two-year centred running mean as above (Fig. 5c).

Meteorological station records. To complement and extend the reanalysis record, Fig. 5c also includes MSLP data from Novolazarevskaya Station on the Queen Maud Land coast of Antarctica (71° S, 12° E; location marked in Fig. 1a; data available from 1972–2019). Monthly means were obtained from the Reference Antarctic Data for Environmental Research (READER) archive[110]. For comparison, Extended Data Fig. 9b shows monthly mean MSLP from the nearby Neumayer (71° S, 8° W; 1981–2019) and Syowa (69° S, 40° E; 1957–2019) Stations from the READER archive and from Maitri Station (71° S, 12° E; 1990–2019), South African National Antarctic Expedition Station (SANAE; 70° S, 2° W; 1973–1994), and SANAE-Automatic Weather Station (SANAE-AWS; 72° S, 3° W; 1997–2019), obtained as subdaily records from the NOAA-NCEI Integrated Surface Database (ISD)[111]. The first two years of the Neumayer and SANAE-AWS records were dropped owing to sparse data and quality issues. As above, two-year centred running means are presented. We observe consistent fluctuations between the station records. Strong correlation between Novolazarevskaya and the Weddell Low

($r = 0.84$; see Extended Data Table 1) suggests that the former is a useful proxy for the latter during the pre-ERA-I period.

Storm identification. A high degree of similarity between six-hourly MSLP from SANAE-AWS, south of Maud Rise, and the nearest ERA-I grid cell from 1997–2019 ($r = 0.93$; mean absolute deviation = 2.2 hPa; mean bias = 0.8 hPa) suggests that ERA-I skilfully represents variability near Maud Rise associated with synoptic-scale weather systems. Validation with independent pressure data from drifting ice buoys in the Bellingshausen Sea also suggests that ERA-I is skilled at capturing individual storms in the Southern Ocean, particularly relative to other available reanalyses[112]. We identify the passage of particularly intense cyclones within the Maud Rise (Figs. 2a, 3a) and eastern Weddell (Fig. 5d) regions. Previous work indicates that storms with a central pressure below 950 hPa represent the most extreme 5% of individually tracked cyclones at a latitude of 65° S[113]. Adopting this pressure threshold, we find (coincidentally) that 5.3% of ERA-I six-hourly MSLP fields feature one or more grid cells below 950 hPa within the eastern Weddell region. Statistically, this corresponds to a wind speed threshold of about 20 m s^{-1}, which is exceeded in 5.8% of instantaneous six-hourly fields. Days on which either criteria are met are designated 'storm days' (see Extended Data Fig. 4). These are denoted by vertical bars in Figs. 2a, 3a, Extended Data Fig. 3a and counted annually during ice-covered winter (May to October) in Fig. 5d. In plots spanning 2016 and 2017, sequences of storm days separated by a single non-storm day are aggregated for ease of visualization.

Data availability

The data analysed in this article are all publicly available, with the exception of updates to the UW Calibrated O_2 package, described below:

Ocean bathymetry data were obtained from the ETOPO1 1 Arc-Minute Global Relief Model[114] at https://doi.org/10.7289/V5C8276M (accessed February 2017).

Sea ice concentration data were obtained for the period 1972–1977 from the NSIDC Nimbus-5 ESMR v1 product[53] at https://doi.org/10.5067/W2PKTWMTY0TP (accessed February 2017); for the period 1978–2017 from the merged NASA Goddard v3 product[54] at https://doi.org/10.7265/N59P2ZTG (accessed October 2018); for January 2018–February 2019 from the NOAA/NSIDC Near-Real-Time CDR v1 product[56] at https://doi.org/10.7265/N5FF3QJ6 (accessed February 2019); and for the period 2002–2019 from the University of Bremen ASI AMSR-E and AMSR2 v5 products[57,58] at https://seaice.uni-bremen.de/sea-ice-concentration/ (accessed February 2019).

Profiling float temperature and salinity measurements were obtained from the US-GODAE GDAC[70] at http://www.usgodae.org/ftp/outgoing/argo (accessed October 2018). Dissolved oxygen measurements for floats 5904468 and 5904471 were obtained from the SOCCOM quality-controlled archive[74] at https://doi.org/10.6075/J02J6968 (accessed January 2019) and for float 5903616 from the UW Calibrated O_2 package, v1.1[75] at http://runt.ocean.washington.edu/o2 (accessed August 2016), with updated dissolved oxygen profiles provided by R. Drucker (personal communication, August 2017).

Shipboard and elephant seal temperature and salinity measurements were obtained from the World Ocean Database 2018 prerelease[77] with August 2018 additions at http://www.nodc.noaa.gov/OC5/SELECT/dbsearch/dbsearch.html (accessed October 2018).

Gridded climatological ocean temperature fields were obtained from the 2018 WAGHC[91] at http://icdc.cen.uni-hamburg.de/1/daten/ocean/waghc (accessed January 2018).

The monthly SAM index[98] was obtained for the period 1972–2019 at http://legacy.bas.ac.uk/met/gjma/sam.html (accessed February 2019).

Monthly and daily ERA-I atmospheric reanalysis fields[99] were obtained for the period 1979–2018 using the Python MARS API, described at https://confluence.ecmwf.int/display/WEBAPI/ (accessed February 2019).

Queen Maud Land pressure records (see Methods section 'Meteorological station records') were obtained from the READER archive[110] at http://legacy.bas.ac.uk/met/READER (accessed February 2019) and the NOAA-NCEI ISD[111] at http://www.ncdc.noaa.gov/isd (accessed February 2019).

Code availability

Analytical scripts used to generate the figures in this paper are available at https://github.com/ethan-campbell.

51. Muench, R. D. et al. Maud Rise revisited. *J. Geophys. Res.* **106**, 2423–2440 (2001).
52. Meier, W. N., Gallaher, D. & Campbell, G. G. New estimates of Arctic and Antarctic sea ice extent during September 1964 from recovered Nimbus I satellite imagery. *Cryosphere* **7**, 699–705 (2013).
53. Parkinson, C. L., Comiso, J. C. & Zwally, H. J. *Nimbus-5 ESMR Polar Gridded Sea Ice Concentrations* v.1 https://doi.org/10.5067/W2PKTWMTY0TP (National Snow and Ice Data Center, 2004).
54. Meier, W. N. et al. *NOAA/NSIDC Climate Data Record of Passive Microwave Sea Ice Concentration* v.3 https://doi.org/10.7265/N59P2ZTG (National Snow and Ice Data Center, 2017).
55. Meier, W. N., Peng, G., Scott, D. J. & Savoie, M. H. Verification of a new NOAA/NSIDC passive microwave sea-ice concentration climate record. *Polar Res.* **33**, https://doi.org/10.3402/polar.v33.21004 (2014).
56. Meier, W. N., Fetterer, F. & Windnagel, A. K. *Near-Real-Time NOAA/NSIDC Climate Data Record of Passive Microwave Sea Ice Concentration* v.1 https://doi.org/10.7265/N5FF3QJ6 (National Snow and Ice Data Center, 2017).
57. Spreen, G., Kaleschke, L. & Heygster, G. Sea ice remote sensing using AMSR-E 89-GHz channels. *J. Geophys. Res. Oceans* **113**, 1–14 (2008).
58. Beitsch, A., Kaleschke, L. & Kern, S. Investigating high-resolution AMSR2 sea ice concentrations during the February 2013 fracture event in the Beaufort Sea. *Remote Sens.* **6**, 3841–3856 (2014).
59. JCOMM Expert Team on Sea Ice. *Sea-Ice Nomenclature*. WMO No. 259 (World Meteorological Organization, 2014).
60. Comiso, J. C., Cavalieri, D. J., Parkinson, C. L. & Gloersen, P. Passive microwave algorithms for sea ice concentration: a comparison of two techniques. *Remote Sens. Environ.* **60**, 357–384 (1997).
61. Comiso, J. C. & Steffen, K. Studies of Antarctic sea ice concentrations from satellite data and their applications. *J. Geophys. Res. Oceans* **106**, 31361–31385 (2001).
62. Comiso, J. C. & Gordon, A. L. Cosmonaut polynya in the Southern Ocean: structure and variability. *J. Geophys. Res. Oceans* **101**, 18297–18313 (1996).
63. Arbetter, T. E., Lynch, A. H. & Bailey, D. A. Relationship between synoptic forcing and polynya formation in the Cosmonaut Sea: 1. Polynya climatology. *J. Geophys. Res.* **109**, C04022 (2004).
64. Gordon, A. L. in *Elsevier Oceanography Series: Deep Convection and Deep Water Formation in the Oceans* Vol. 57 (eds. Chu, P. C. & Gascard, J.-C.) 17–35 (Elsevier, 1991).
65. Venegas, S. A. & Drinkwater, M. R. Sea ice, atmosphere and upper ocean variability in the Weddell Sea, Antarctica. *J. Geophys. Res.* **106**, 16747–16765 (2001).
66. Riser, S. C. et al. Fifteen years of ocean observations with the global Argo array. *Nat. Clim. Change* **6**, 145–153 (2016).
67. Riser, S. C., Swift, D. & Drucker, R. Profiling floats in SOCCOM: technical capabilities for studying the Southern Ocean. *J. Geophys. Res. Oceans* **123**, 4055–4073 (2018).
68. Klatt, O., Boebel, O. & Fahrbach, E. A profiling float's sense of ice. *J. Atmos. Ocean. Technol.* **24**, 1301–1308 (2007).
69. Wong, A. P. S. & Riser, S. C. Profiling float observations of the upper ocean under sea ice off the Wilkes Land coast of Antarctica. *J. Phys. Oceanogr.* **41**, 1102–1115 (2011).
70. Carval, T. et al. *Argo User's Manual* v. 3.2 (Argo, 2017).
71. Chamberlain, P. M. et al. Observing the ice-covered Weddell Gyre with profiling floats: position uncertainties and correlation statistics. *J. Geophys. Res. Oceans* **123**, 8383–8410 (2018).
72. Meredith, M. P. et al. Circulation, retention, and mixing of waters within the Weddell-Scotia Confluence, Southern Ocean: The role of stratified Taylor columns. *J. Geophys. Res. Oceans* **120**, 547–562 (2015).
73. Talley, L. D. et al. Southern Ocean biogeochemical float deployment strategy, with example from the Greenwich Meridian line (GO-SHIP A12). *J. Geophys. Res. Oceans* **124**, 403–431 (2019).
74. Johnson, K. S. et al. *Southern Ocean Carbon and Climate Observations and Modeling (SOCCOM) Float Data Archive - Snapshot 2018-12-31*, https://doi.org/10.6075/J02J6968 (UC San Diego, 2019).
75. Drucker, R. & Riser, S. C. In situ phase-domain calibration of oxygen Optodes on profiling floats. *Methods Oceanogr.* **17**, 296–318 (2016).
76. Johnson, K. S. et al. Biogeochemical sensor performance in the SOCCOM profiling float array. *J. Geophys. Res. Oceans* **122**, 6416–6436 (2017).
77. Boyer, T. P. et al. *World Ocean Database 2018*. NOAA Atlas NESDIS 87 (NOAA, 2018).
78. Roquet, F. et al. A Southern Indian Ocean database of hydrographic profiles obtained with instrumented elephant seals. *Sci. Data* **1**, 140028 (2014).
79. Boehme, L. et al. Animal-borne CTD-Satellite Relay Data Loggers for real-time oceanographic data collection. *Ocean Sci.* **5**, 685–695 (2009).
80. Siegelman, L. et al. Correction and accuracy of high- and low-resolution CTD data from animal-borne instruments. *J. Atmos. Ocean. Technol.* **36**, 745–760 (2019).
81. de Boyer Montégut, C., Madec, G., Fischer, A. S., Lazar, A. & Iudicone, D. Mixed layer depth over the global ocean: an examination of profile data and a profile-based climatology. *J. Geophys. Res.* **109**, C12003 (2004).
82. Dong, S., Sprintall, J., Gille, S. T. & Talley, L. Southern Ocean mixed-layer depth from Argo float profiles. *J. Geophys. Res.* **113**, C06013 (2008).
83. Marshall, J. & Schott, F. Open-ocean convection: observations, theory, and models. *Rev. Geophys.* **37**, 1–64 (1999).
84. Margirier, F. et al. Characterization of convective plumes associated with oceanic deep convection in the northwestern Mediterranean from high-resolution in situ data collected by gliders. *J. Geophys. Res. Oceans* **122**, 9814–9826 (2017).
85. Haumann, F. A., Gruber, N., Münnich, M., Frenger, I. & Kern, S. Sea-ice transport driving Southern Ocean salinity and its recent trends. *Nature* **537**, 89–92 (2016).
86. Charrassin, J.-B. et al. Southern Ocean frontal structure and sea-ice formation rates revealed by elephant seals. *Proc. Natl Acad. Sci. USA* **105**, 11634–11639 (2008).

87. Bailey, D. A., Rhines, P. B. & Häkkinen, S. Formation and pathways of North Atlantic Deep Water in a coupled ice–ocean model of the Arctic–North Atlantic Oceans. *Clim. Dyn.* **25**, 497–516 (2005).
88. Frajka-Williams, E., Rhines, P. B. & Eriksen, C. C. Horizontal stratification during deep convection in the Labrador Sea. *J. Phys. Oceanogr.* **44**, 220–228 (2014).
89. Pellichero, V., Sallée, J.-B., Schmidtko, S., Roquet, F. & Charrassin, J.-B. The ocean mixed layer under Southern Ocean sea-ice: seasonal cycle and forcing. *J. Geophys. Res. Oceans* **122**, 1608–1633 (2017).
90. Talley, L. D., Pickard, G. L., Emery, W. J. & Swift, J. H. *Descriptive Physical Oceanography: An Introduction* Ch. 7, 187–222 (Elsevier, 2011).
91. Gouretski, V. World Ocean Circulation Experiment – Argo Global Hydrographic Climatology. *Ocean Sci.* **14**, 1127–1146 (2018).
92. Fahrbach, E. et al. Warming of deep and abyssal water masses along the Greenwich meridian on decadal time scales: the Weddell gyre as a heat buffer. *Deep Sea Res. Part II* **58**, 2509–2523 (2011).
93. Ryan, S., Schröder, M., Huhn, O. & Timmermann, R. On the warm inflow at the eastern boundary of the Weddell Gyre. *Deep Sea Res. Part I* **107**, 70–81 (2016).
94. Smedsrud, L. H. Warming of the deep water in the Weddell Sea along the Greenwich meridian: 1977–2001. *Deep Sea Res. Part I* **52**, 241–258 (2005).
95. Fahrbach, E., Hoppema, M., Rohardt, G., Schröder, M. & Wisotzki, A. Causes of deep-water variation: comment on the paper by L.H. Smedsrud "Warming of the deep water in the Weddell Sea along the Greenwich meridian: 1977–2001". *Deep Sea Res. Part I* **53**, 574–577 (2006).
96. Gordon, A. L. Weddell Deep Water variability. *J. Mar. Res.* **40**, 199–217 (1982).
97. Zanowski, H. & Hallberg, R. Weddell Polynya transport mechanisms in the abyssal ocean. *J. Phys. Oceanogr.* **47**, 2907–2925 (2017).
98. Marshall, G. J. Trends in the Southern Annular Mode from observations and reanalyses. *J. Clim.* **16**, 4134–4143 (2003).
99. Dee, D. P. et al. The ERA-Interim reanalysis: configuration and performance of the data assimilation system. *Q. J. R. Meteorol. Soc.* **137**, 553–597 (2011).
100. Sumata, H. et al. An intercomparison of Arctic ice drift products to deduce uncertainty estimates. *J. Geophys. Res. Oceans* **119**, 4887–4921 (2014).
101. Martinson, D. G. & Wamser, C. Ice drift and momentum exchange in winter Antarctic pack ice. *J. Geophys. Res.* **95**, 1741–1755 (1990).
102. Wang, Z., Turner, J., Sun, B., Li, B. & Liu, C. Cyclone-induced rapid creation of extreme Antarctic sea ice conditions. *Sci. Rep.* **4**, 5317 (2015).
103. Kottmeier, C. & Sellmann, L. Atmospheric and oceanic forcing of Weddell Sea ice motion. *J. Geophys. Res. Oceans* **101**, 20809–20824 (1996).
104. Fairall, C. W., Bradley, E. F., Rogers, D. P., Edson, J. B. & Young, G. S. Bulk parameterization of air-sea fluxes for Tropical Ocean-Global Atmosphere Coupled-Ocean Atmosphere Response Experiment. *J. Geophys. Res. Oceans* **101**, 3747–3764 (1996).
105. Renfrew, I. A., Moore, G. W. K., Guest, P. S. & Bumke, K. A comparison of surface layer and surface turbulent flux observations over the Labrador Sea with ECMWF analyses and NCEP reanalyses. *J. Phys. Oceanogr.* **32**, 383–400 (2002).
106. Holland, P. R. & Kwok, R. Wind-driven trends in Antarctic sea-ice drift. *Nat. Geosci.* **5**, 872–875 (2012).
107. Jullion, L., Jones, S. C., Naveira Garabato, A. C. & Meredith, M. P. Wind-controlled export of Antarctic Bottom Water from the Weddell Sea. *Geophys. Res. Lett.* **37**, L09609 (2010).
108. Meijers, A. J. S. et al. Wind-driven export of Weddell Sea slope water. *J. Geophys. Res. Oceans* **121**, 7530–7546 (2016).
109. Armitage, T. W. K., Kwok, R., Thompson, A. F. & Cunningham, G. Dynamic topography and sea level anomalies of the Southern Ocean: variability and teleconnections. *J. Geophys. Res. Oceans* **123**, 613–630 (2018).
110. Turner, J. et al. The SCAR READER project: toward a high-quality database of mean Antarctic meteorological observations. *J. Clim.* **17**, 2890–2898 (2004).
111. Smith, A., Lott, N. & Vose, R. The Integrated Surface Database: recent developments and partnerships. *Bull. Am. Meteorol. Soc.* **92**, 704–708 (2011).
112. Bracegirdle, T. J. Climatology and recent increase of westerly winds over the Amundsen Sea derived from six reanalyses. *Int. J. Climatol.* **33**, 843–851 (2013).
113. Patoux, J., Yuan, X. & Li, C. Satellite-based midlatitude cyclone statistics over the Southern Ocean: 1. Scatterometer-derived pressure fields and storm tracking. *J. Geophys. Res.* **114**, D04105 (2009).
114. Amante, C. & Eakins, B. W. *ETOPO1 1 Arc-Minute Global Relief Model: Procedures, Data Sources and Analysis.* NOAA Technical Memorandum NESDIS NGDC-24 (National Geophysical Data Center, 2009) https://doi.org/10.7289/V5C8276M.

Acknowledgements We thank A. Wong, R. Drucker, J. Plant, T. Maurer and K. Johnson for assistance with float data calibration, and all others involved in float and sensor design, construction, calibration and deployment for their contributions. Data were collected and made freely available by the Southern Ocean Carbon and Climate Observations and Modeling (SOCCOM) Project, which is funded by the US National Science Foundation, Division of Polar Programs (NSF PLR-1425989), supplemented by NASA, and by the International Argo Program and the NOAA programmes that contribute to it. The Argo Program is part of the Global Ocean Observing System. E.C.C. acknowledges funding from the University of Washington (UW) Program on Climate Change, ARCS Foundation, and US Department of Defense through the National Defense Science & Engineering Graduate (NDSEG) Fellowship Program. E.A.W., S.C.R., M.R.M. and L.D.T. acknowledge funding from NSF PLR-1425989, and S.C.R. from NOAA grant NA15OAR4320063. G.W.K.M. acknowledges the support of the Canada Fulbright Foundation, UW Jackson School of International Studies, and the Natural Sciences and Engineering Research Council of Canada. C.E.B. was supported by the Scripps Undergraduate Research Fellowship (SURF) programme.

Author contributions E.C.C., E.A.W. and S.C.R. conceived the study and E.C.C. wrote the initial manuscript. E.C.C. and E.A.W. analysed the hydrographic data and together with G.W.K.M. analysed the sea ice and reanalysis data. S.C.R. led the float design and construction and together with L.D.T. coordinated SOCCOM float deployments. All authors interpreted results and provided input to the final manuscript.

Competing interests The authors declare no competing interests.

Additional information

Correspondence and requests for materials should be addressed to E.C.C.

Peer review information *Nature* thanks Céline Heuzé, Lars Henrik Smedsrud and the other anonymous reviewer(s) for their contribution to the peer review of this work.

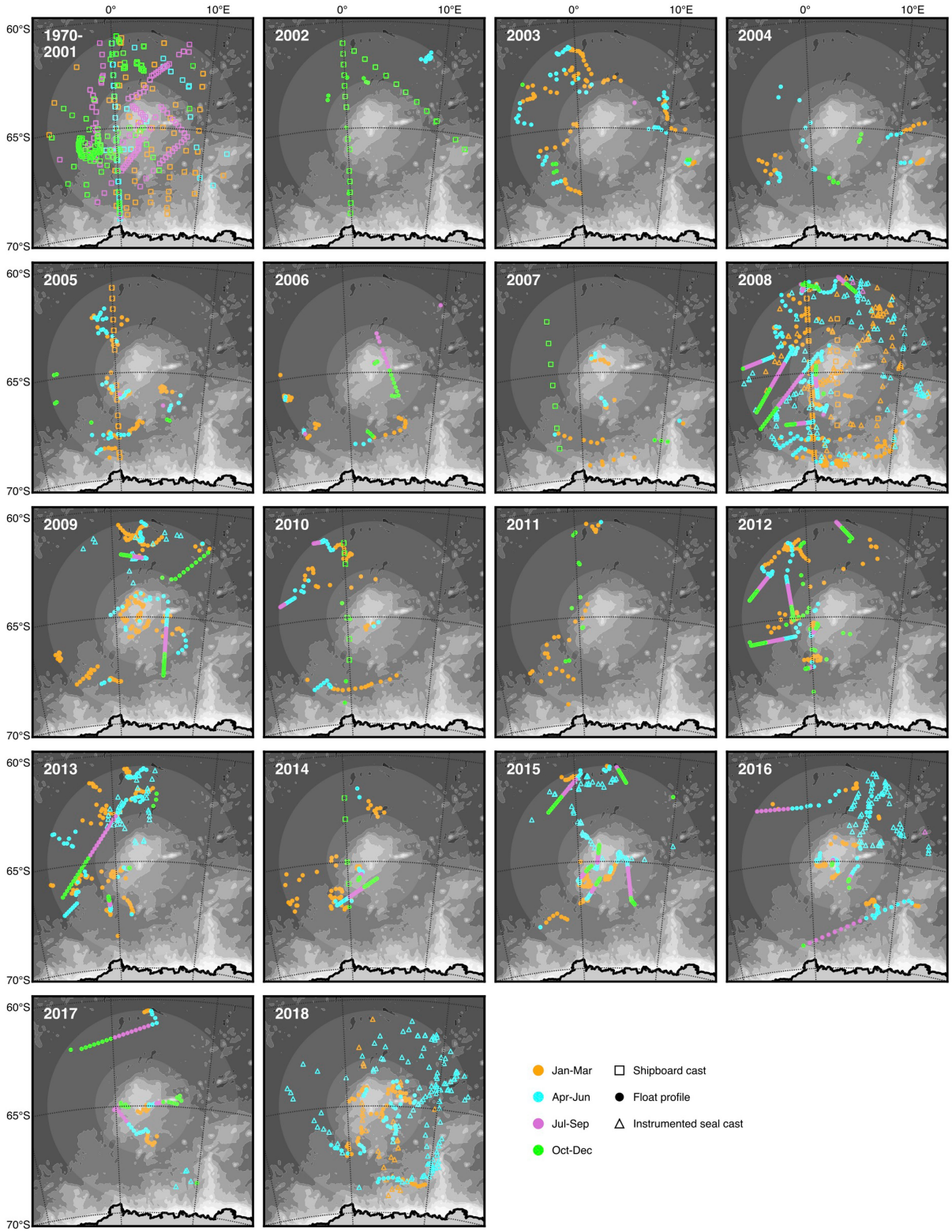

Extended Data Fig. 1 | Locations of observations used to construct hydrographic climatologies for the Maud Rise and eastern Weddell regions. Observations from 1970 to 2001 are shown together (top left); observations from 2002 to 2018 are represented by one panel per year. Included are float profiles from the Argo GDAC (filled circles) as well as shipboard (open squares) and instrumented seal (open triangles) casts from the World Ocean Database (see Methods section 'Hydrographic data'). Colours indicate seasons. Bathymetric contours (intervals of 750 m) highlight Maud Rise and the Antarctic continental shelf. Concentric circles represent radii of 250 km and 500 km from Maud Rise, encompassing the Maud Rise and eastern Weddell regions, respectively (see Methods section 'Regions').

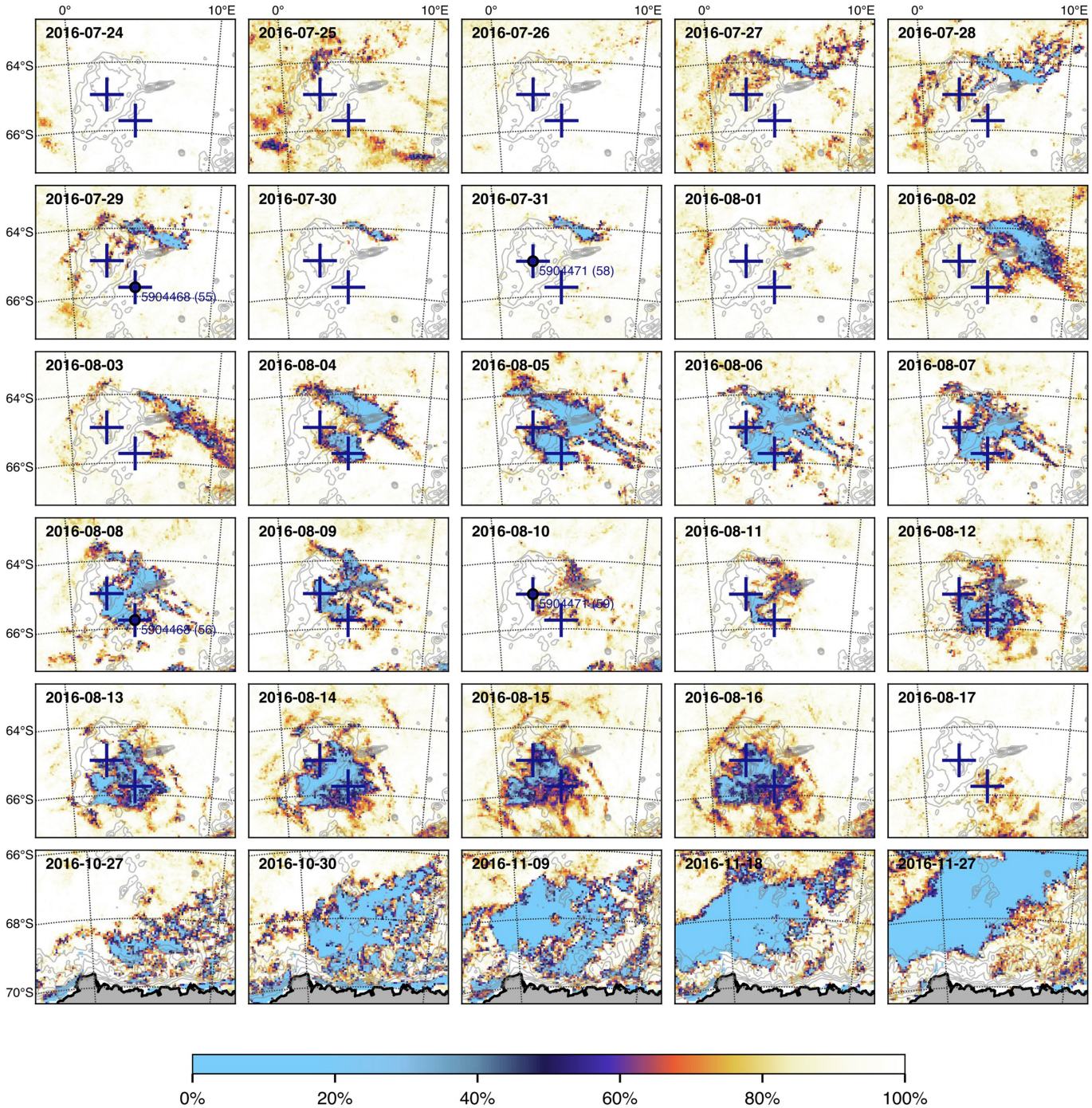

Extended Data Fig. 2 | Sea ice concentration during the 2016 polynya. Daily SIC from AMSR2-ASI around Maud Rise from 24 July to 17 August 2016, encompassing the main polynya event, followed by selected SIC fields from AMSR2-ASI during the late-winter 2016 polynya south of Maud Rise (bottom row; note different map area). Estimated locations of SOCCOM profiling floats 5904471 and 5904468 (see Methods section 'Hydrographic data') are marked in blue; a circle marker and profile number indicate that a hydrographic profile was obtained on that date. Bathymetry shallower than 3,500 m is contoured at intervals of 500 m to highlight Maud Rise (centre of July–August images) as well as Astrid Ridge (bottom right of October–November images), an extension of the Antarctic continental shelf.

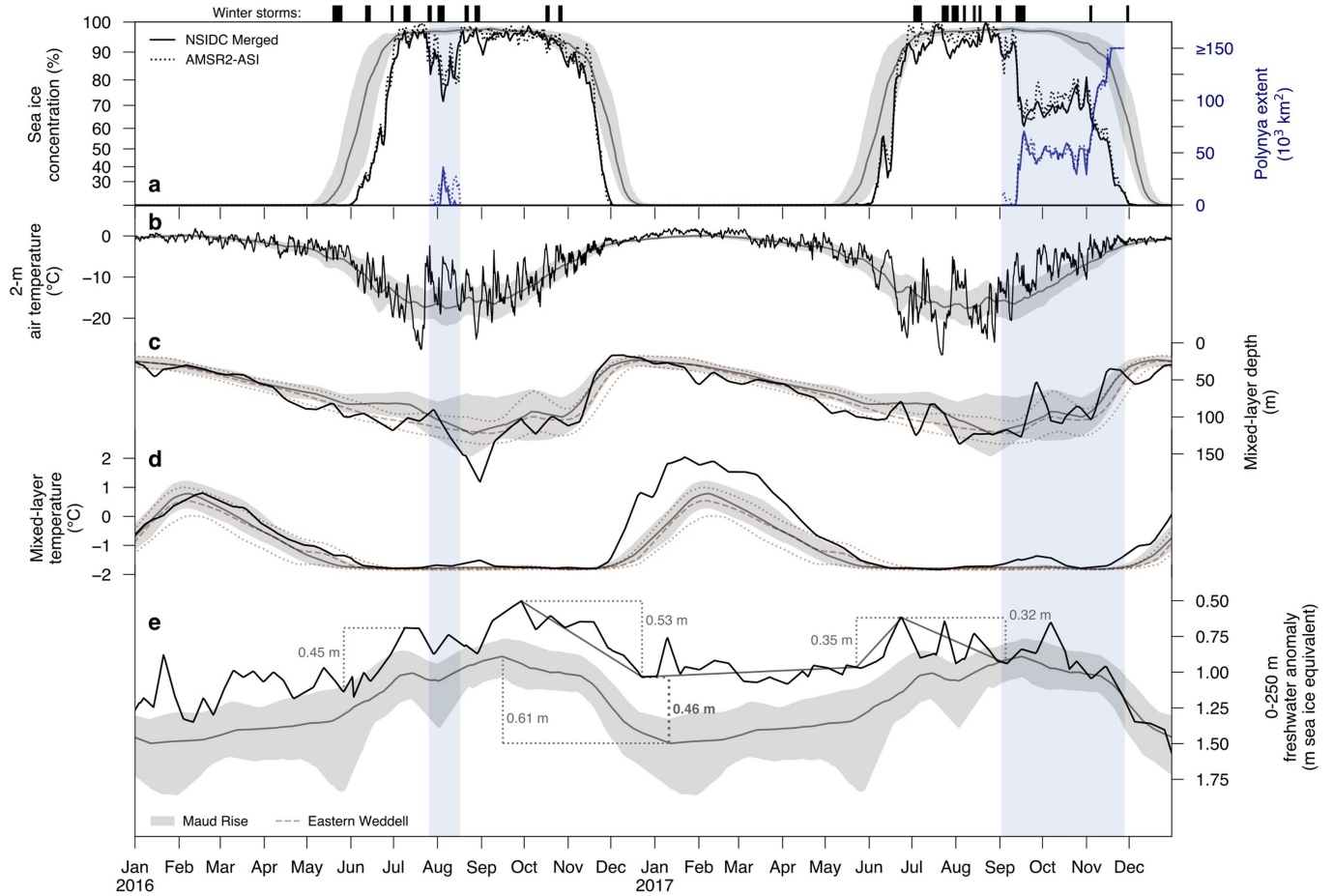

Extended Data Fig. 3 | Evolution of sea ice concentration, air temperature and upper ocean properties at Maud Rise in 2016 and 2017. Marked at the top are intense winter storm events near Maud Rise, as in Fig. 2 (also see Extended Data Fig. 4 and Methods section 'Storm identification'). **a**, Average daily SIC within the Maud Rise region (63°–67° S, 0°–10° E) from NSIDC Merged (solid black line) and AMSR2-ASI (dashed black line) in 2016 and 2017, as in Fig. 2a. SIC climatology from NSIDC Merged (1978–2019) is shown as median (grey line) and 25–75% interquartile range (IQR; grey shading). Note the stretched *y* axis. Polynya extent is quantified (blue lines) during the 2016 and 2017 events (vertical blue shading). **b**, Six-hourly 2-m air temperature around Maud Rise (within 63°–67° S, 0°–10° E) from ERA-I reanalysis (black line). Climatology for 1979–2018 is shown as mean (grey line) and IQR (grey shading). **c**, Composite of average MLD in 2016 and 2017 measured by floats 5903616, 5904468 and 5904471 (black line; see Methods sections 'Derived oceanographic quantities' and 'Composites of float time series'). MLD climatology for the Maud Rise region ($R < 250$ km from 65° S, 3° E) is shown as median (grey line) and IQR (grey shading); climatology for the eastern Weddell region away from Maud Rise ($250 < R < 500$ km) is presented for comparison (light brown dashed and dotted lines for median and IQR, respectively; see Methods section 'Hydrographic climatologies'). **d**, Composite of average mixed-layer potential temperature (MLT) and MLT climatology presented as in **c**. **e**, Composite of the lowest observed upper-250-m freshwater anomaly (or 'salt deficit'; see Methods sections 'Derived oceanographic quantities' and 'Composites of float time series') and freshwater anomaly climatology for the Maud Rise region presented as in **c**. Note the reversed *y* axis. Key changes quantified, from left to right, are 2016 freeze, climatological melt, 2016 melt, anomaly from climatology in January 2017, 2017 freeze, and change between 2017 freeze and 2017 polynya appearance.

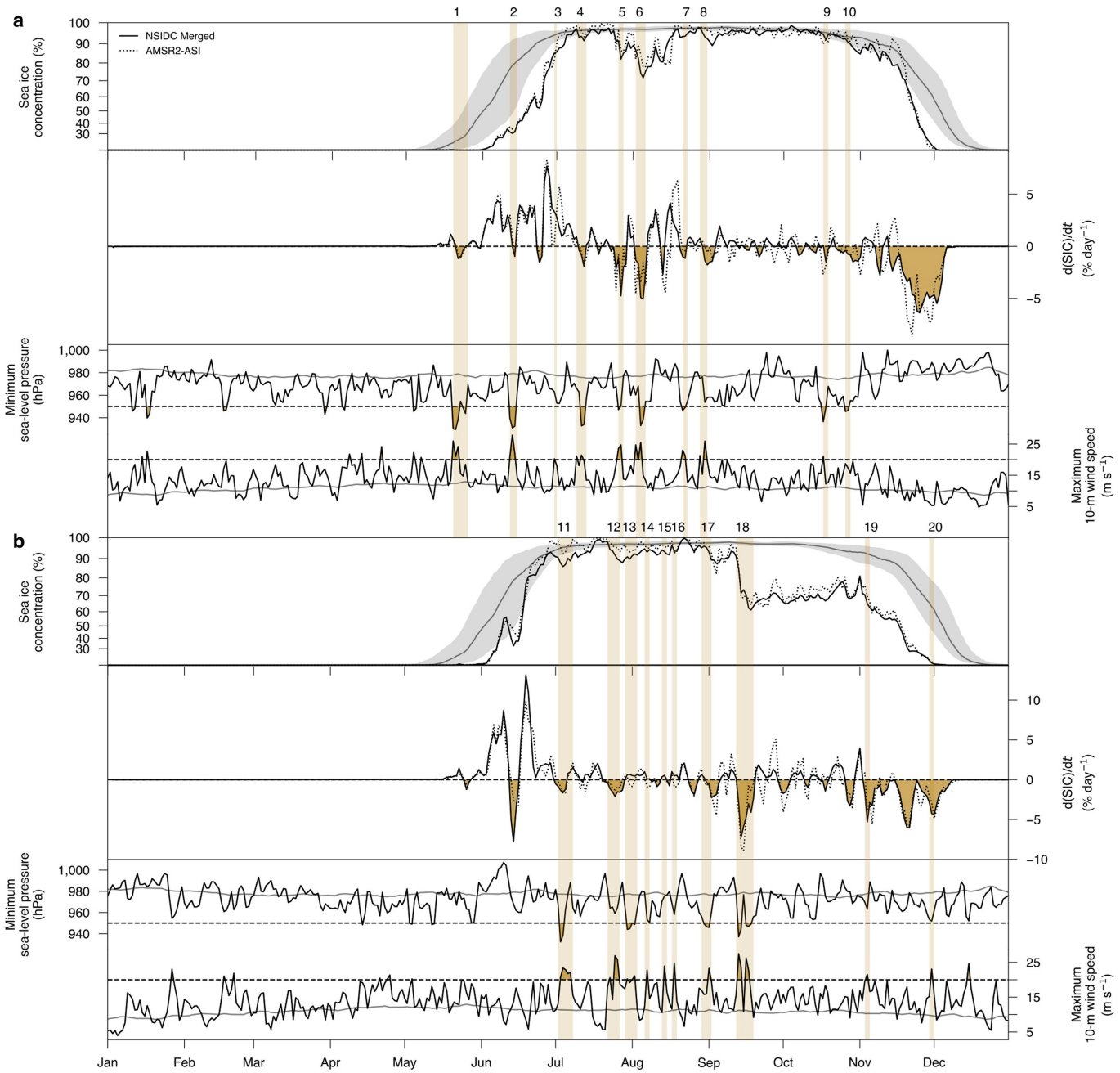

Extended Data Fig. 4 | Correspondence of sea ice loss episodes and major storms near Maud Rise. a, **b**, Time series are shown for 2016 (**a**) and 2017 (**b**). Average daily SIC within the Maud Rise region (63°–67° S, 0°–10° E) from NSIDC Merged (solid black line) and AMSR2-ASI (dashed black line) is presented at the top for each year, as in Fig. 2a. SIC climatology from NSIDC Merged (1978–2019) is shown as median (grey line) and 25–75% interquartile range (grey shading). Note the stretched *y* axis. Daily changes in SIC are presented in the centre for each year, with negative changes in NSIDC Merged highlighted (dark yellow shading); both NSIDC Merged and AMSR2-ASI time series are smoothed using a 3-day right-edge running-mean filter. At the bottom for each year are the minimum daily sea-level pressure and maximum daily 10-m wind speed near Maud Rise (within 63–67° S, 0–10° E) from ERA-I reanalysis. Mean climatological values of these minimum/maximum metrics are shown (grey lines) to highlight the lack of a pronounced seasonal cycle. The most intense winter polar lows, as shown in Figs. 2, 3, Extended Data Fig. 3, are identified here using pressure and wind speed thresholds (dark yellow shading from dashed lines), and aggregated 'storm days' are numbered at the top and marked with vertical yellow bars (see Methods section 'Storm identification').

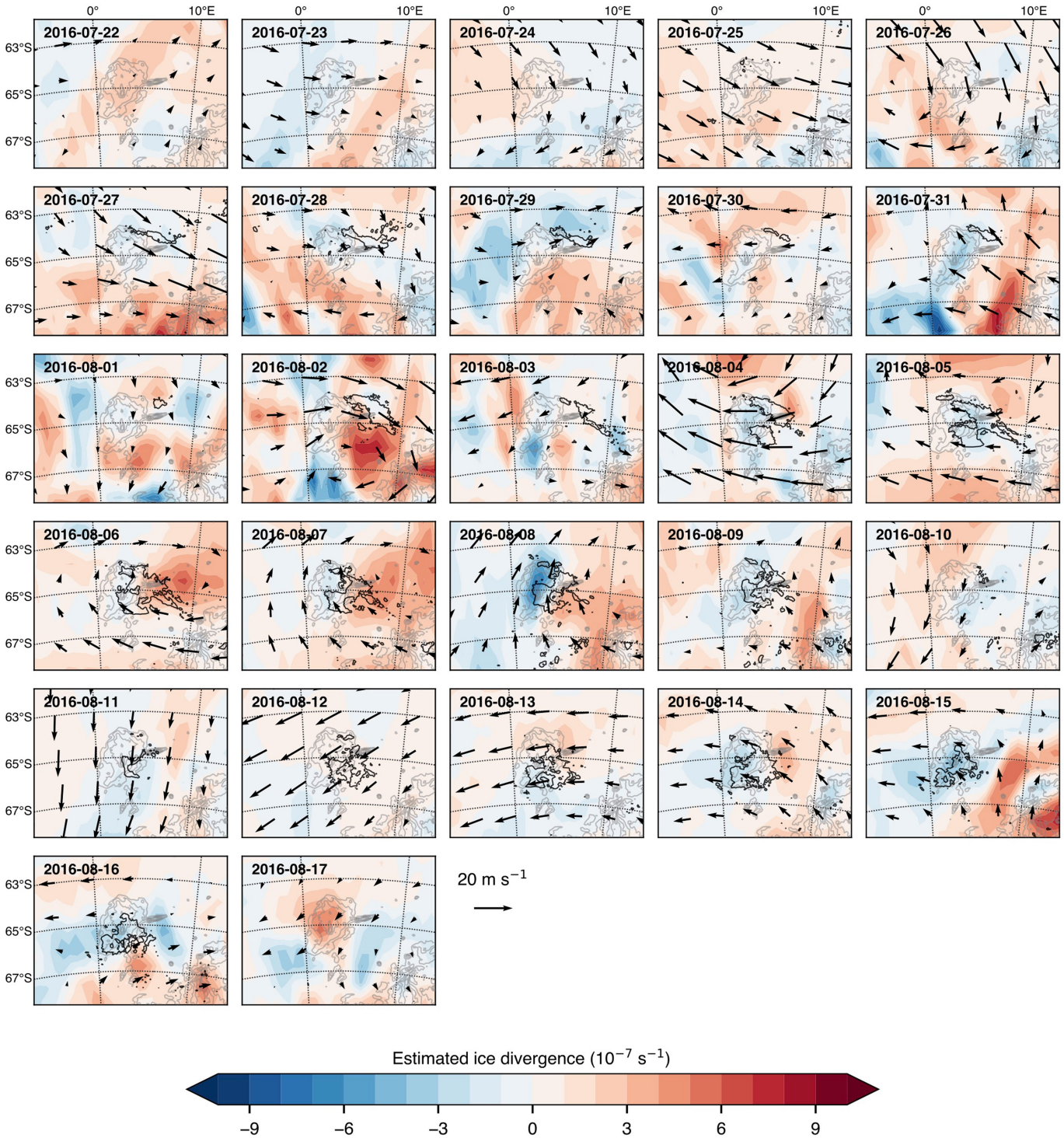

Extended Data Fig. 5 | Winds and wind-induced sea ice divergence during the 2016 polynya. 50% SIC contours (black) from AMSR2-ASI show the daily polynya evolution from 22 July to 17 August 2016. Bathymetry shallower than 3,500 m is contoured at intervals of 500 m (light grey) to highlight Maud Rise (centre). Daily mean 10-m wind vectors from ERA-I reanalysis, subsampled as every fifth u-wind and every second v-wind vector, are plotted with a 20 m s^{-1} key as reference. Estimated daily mean wind-induced sea ice divergence (see Methods section 'Atmospheric reanalysis') is shaded such that red represents divergence and blue represents convergence.

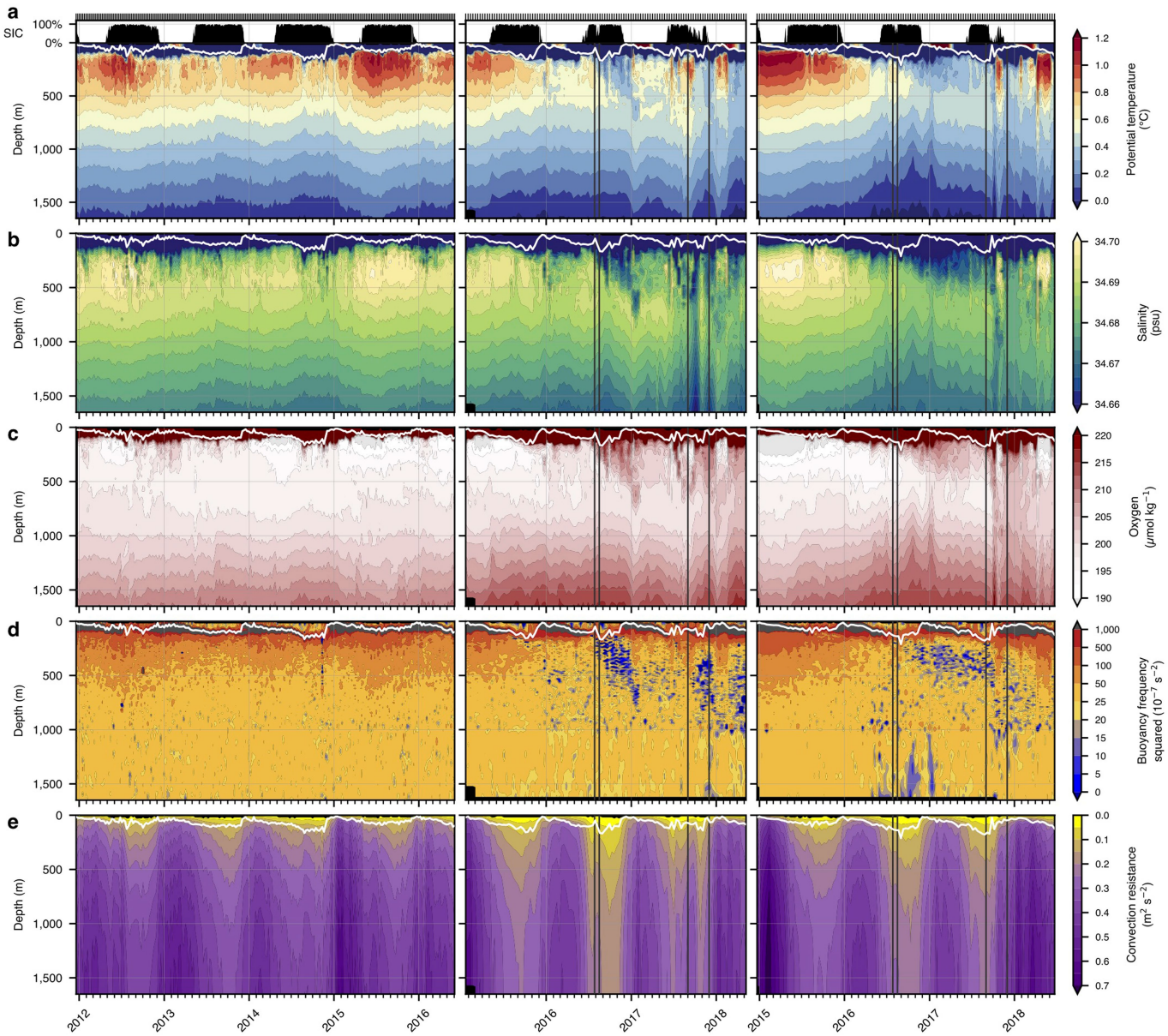

Extended Data Fig. 6 | Full set of profiling float hydrographic observations from Maud Rise from 2011–2018. a–e, Complete depth sections of potential temperature (**a**), salinity (**b**), dissolved oxygen (**c**), buoyancy frequency squared (N^2) (**d**) and convection resistance (see Methods section 'Derived oceanographic quantities') (**e**) from profiling floats 5903616 (left), 5904468 (centre) and 5904471 (right), as shown in Fig. 4. Individual profiles are marked at the top (black ticks). Mixed-layer depth is indicated in white. Vertical lines in each panel mark the start and end dates of the 2016 and 2017 polynyas. Along-trajectory SIC, primarily from AMSR2-ASI, is shaded at the top in black (see Methods section 'Sea ice concentration data').

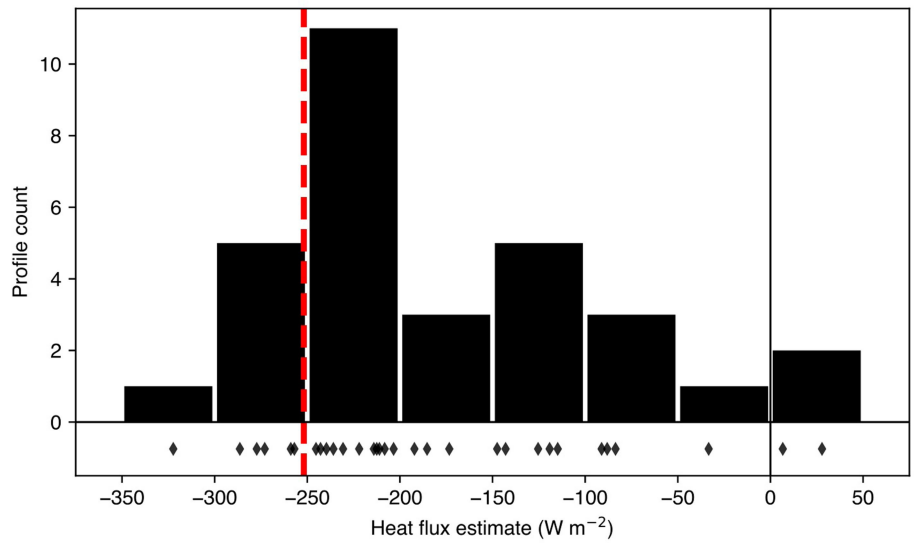

Extended Data Fig. 7 | Heat loss during the 2016 polynya estimated from hydrographic observations. Heat flux estimates ($n = 31$; diamonds at the bottom correspond to histogram above) computed using potential temperature profiles from floats 5904468 and 5904471 following the opening of the 2016 polynya (see Methods section 'Polynya heat flux estimates'). The dashed red line marks the average open-water ocean-atmosphere turbulent heat flux within the 2016 opening, estimated using a bulk flux algorithm as 252 W m^{-2} (see Methods section 'Atmospheric reanalysis').

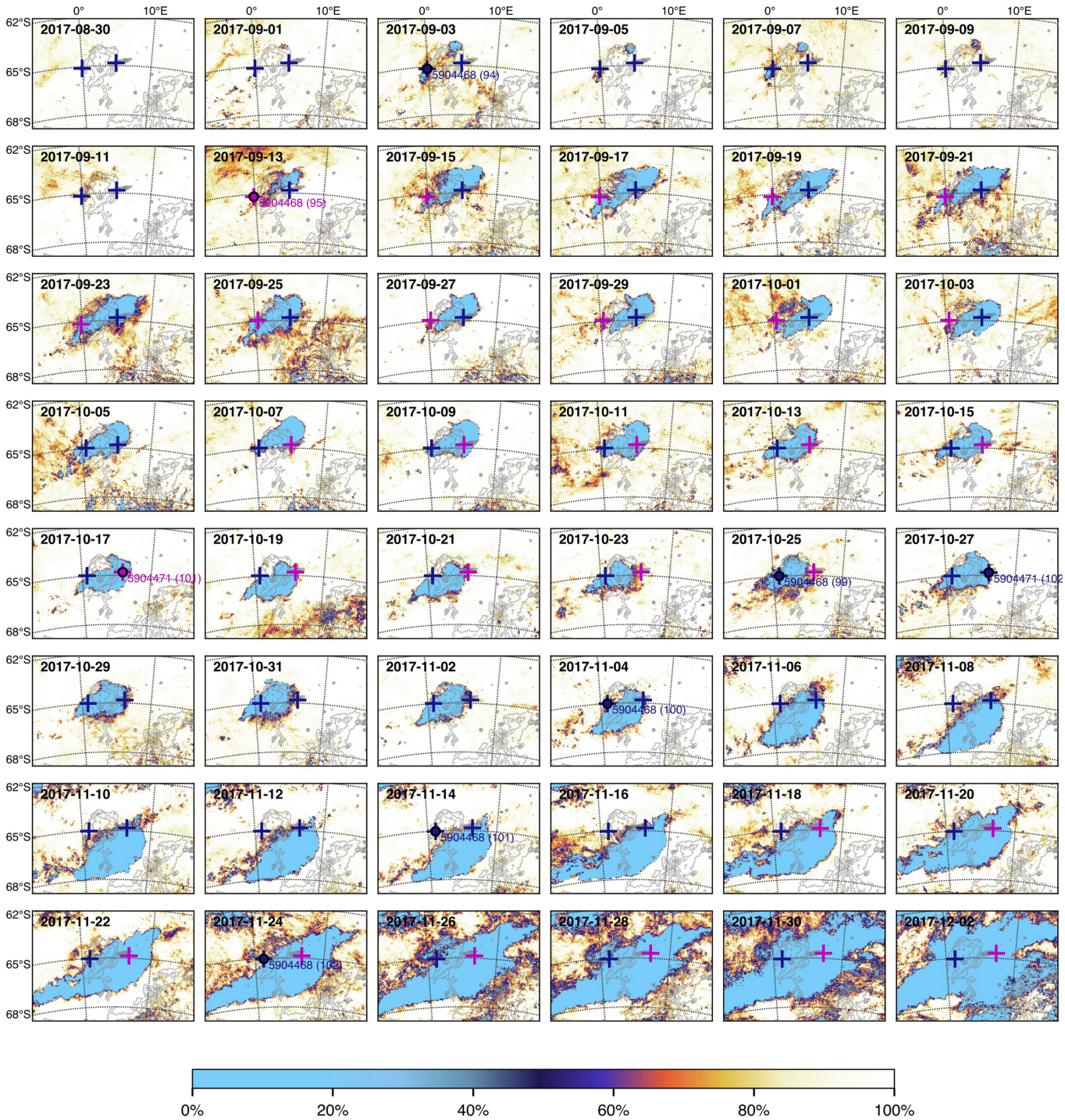

Extended Data Fig. 8 | Sea ice concentration during the 2017 polynya. SIC from AMSR2-ASI around Maud Rise is shown every other day from 30 August to 2 December 2017. Estimated locations of SOCCOM profiling floats 5904471 and 5904468 are marked in blue; locations of profiling floats following an ice-free profile with a known position fix are marked in pink (see Methods section 'Hydrographic data'). A circle marker and profile number indicate that a hydrographic profile was obtained on that date. Bathymetry shallower than 3,500 m is contoured at intervals of 500 m to highlight Maud Rise (centre) as well as Astrid Ridge (bottom right), an extension of the Antarctic continental shelf.

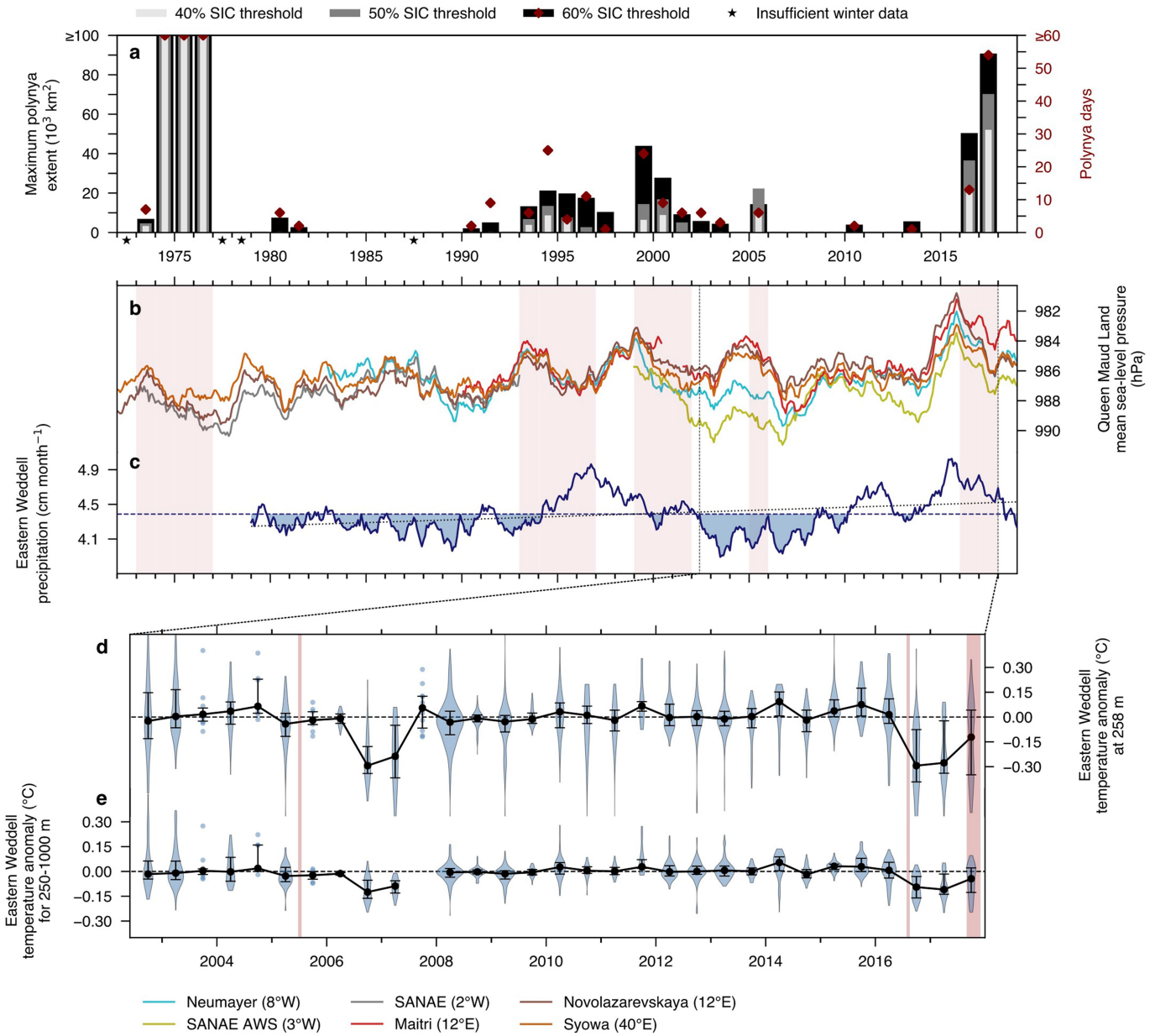

Extended Data Fig. 9 | Additional relationships between past polynyas near Maud Rise, climate forcing, and sub-pycnocline temperatures. **a**, Annual maximum polynya extent (bars) and number of polynya days (red diamonds; see Methods section 'Polynya identification'), as in Fig. 5a. Maximum polynya extent is calculated for three SIC thresholds representing increasingly strict polynya definitions: 60%, 50% and 40%. Polynya days are quantified using the 60% threshold. Stars indicate years with incomplete or absent SIC records. Years with polynya activity at the 50% threshold are shaded vertically in red in **b**, **c**, and likewise in **d**, **e**, except vertical shading delimits the actual major polynya events. **b**, Mean sea-level pressure records from Queen Maud Land meteorological stations, 1972–2018 (see legend and Methods section 'Meteorological station records'). **c**, Eastern Weddell average precipitation from ERA-I reanalysis between 1979 and 2018, shaded below its mean value to indicate years with polynya-favourable conditions (that is, lower atmosphere–ocean freshwater flux), consistent with Fig. 5. Time series in **b** and **c** are filtered using a two-year centred running mean to highlight longer-term fluctuations. **d**, Biannually binned eastern Weddell region (within 500 km of Maud Rise) shipboard, float and instrumented seal temperature observations at 258 m from 2002 to 2017, expressed as anomalies from WAGHC gridded hydrographic climatology (see Methods section 'Sub-pycnocline temperature records'). Error bars denote median and 25–75% IQR. Violin plots summarize the data distribution for $n > 10$, and individual anomalies are shown for $5 \leq n \leq 10$. Periods with $n < 5$ are not plotted. **e**, As in **d**, but showing average temperature anomalies from WAGHC climatology between 250–1,000 m (see Methods section 'Sub-pycnocline temperature records'). See Extended Data Table 1 for trends and significance for **c**–**e**.

Extended Data Table 1 | Correlations and trends for climate indices and sub-pycnocline temperature records

	1	2	3	4	5	6	7	Period	Trend (decade^{-1})	*p*
1 Southern Annular Mode (SAM) index†	1.00 (0)	-0.71 (0)	-0.82 (0)	-0.38 (-1)	-0.51 (0)	0.30 (-1)	0.36 (-1)	1972-2018	0.25	0.00
2 Weddell Low SLP		1.00 (0)	0.84 (0)	0.48 (0)	0.61 (0)	-0.55 (-1)	-0.38 (0)	1979-2018	-0.24 hPa	0.13
3 Novolazarevskaya SLP†			1.00 (0)	0.48 (0)	0.59 (0)	-0.50 (-1)	-0.31 (0)	1972-2018	-0.81 hPa	0.00
4 Maud Rise wind stress curl				1.00 (0)	0.50 (0)	-0.40 (-2)	-0.56 (0)	1979-2018	$-0.07 \cdot 10^{-7}$ N m^{-3}	0.16
5 Weddell gyre wind stress curl†					1.00 (0)	-0.47 (-1)	-0.67 (0)	1979-2018	$-0.05 \cdot 10^{-7}$ N m^{-3}	0.02
6 E. Weddell winter storm days per month*†						1.00 (0)	0.33 (3)	1979-2018	0.50	0.01
7 E. Weddell precipitation							1.00 (0)	1979-2018	0.07 cm month^{-1}	0.15
E. Weddell 258-m temperature anomaly								Jan. 2008 - Jun. 2016	0.07°C	0.04
								Jul. 2002 - Jun. 2016	0.05°C	0.17
E. Weddell 250-1000-m temperature anomaly								Jan. 2008 - Jun. 2016	0.03°C	0.11
								Jul. 2002 - Jun. 2016	0.03°C	0.03

Pearson correlation coefficients (*r*) between climate indices from Fig. 5 and Extended Data Fig. 9 are listed for the lag within ±3 years at which the absolute value of the correlation is maximal. Lags are cited within parentheses in months; positive values indicate the index on the top axis leads and the index on the vertical axis lags. Except where noted (see footnotes), correlations were calculated after applying a 12-month centred running mean to mitigate seasonality, with a minimum filter window of 6 months. Linear trend estimates and significance (*p*) were computed using a two-sided Wald test. At the top right, trends are shown for climate indices, assessed using the original, unfiltered time series. At the bottom right, trends are shown for both the full period of sub-pycnocline temperature anomaly records before the 2016 polynya as well as the subperiod beginning in 2008, calculated using the biannual median values (see Extended Data Fig. 9d, e). We analyse the subperiod beginning in 2008 separately because the amount of float and elephant seal observations within the eastern Weddell region increased sharply that year (Extended Data Fig. 1).

*Six-month (winter only) running mean applied.

†Series detrended (original series found to have significant trend, that is, two-sided $p < 0.05$).